



On the Modelization of Optical Devices From Dielectric Cavities to Radiating Structures

Mémoire

Joey Dumont

Maîtrise en physique
Maître ès sciences (M.Sc.)

Québec, Canada

© Joey Dumont, 2014

Résumé

Abstract

In recent years, outbursts in technology have changed the way we view, and do, science. In the days of yore, when the rose that is physics had not yet been given its name, science was in major part an experimental endeavour. It took the great Werner Heisenberg to establish theoretical physics as its own field. Today, however, it seems that the incredible ease with which we can produce data, throves upon throves of it, has spawned the idea that data is law, that data is self-sufficient, that the throne of theory has been usurped by the opulent and almighty data. In this thesis, we seek to reverse this trend by showing that theoretical analysis can yield physical insights inherently inaccessible to raw data.

We will first investigate the modelization of bidimensional dielectric cavities. The last decade has shown that this type of micron-sized device is ripe with applications ranging from biodetection to lasing action (more on that later). This has motivated the scientific community to investigate the behaviour of such cavities mostly as a function of their geometry, leaving their refractive index profile constant. We will generalize a scattering method that can deal with arbitrary geometry and arbitrary refractive index profiles and provides a way to accurately compute the resonances of such structures.

In the second part, we will discuss the modelization of radiating structures. Using the formalism developed in the previous section, we will study in detail the lasing properties of bidimensional cavities using the newly developed *self-consistent ab initio laser theory* (SALT). We will also attempt to model a class of antenna known as *leaky coax* antennas using a mix of semi-analytic and all-numerical methods. More specifically, we will attempt to explain the experimental data and the simulation data.

Table of Contents

Résumé	iii
Abstract	v
Table of Contents	vii
List of Figures	ix
List of Tables	xi
Notation	xvii
Glossary	xx
Acronyms	xxi
Preface	xxiii
Contributions	xxv
1 Introduction	1
1.1 The Study of Passive Dielectric Microcavities	1
1.2 Onwards to Radiating Structures	4
1.3 Content of this Work	4
2 Passive Media	5
2.1 Maxwell's Equations for Bidimensional Cavities: Reduction from 3D to 2D	5
2.2 Scattering Matrix Formalism	9
2.3 Numerical Implementation	14
2.4 Case Study: Gaussian Deformation of the Refractive Index	22
2.5 Perspectives	24
3 Active Media and Radiation	27
3.1 Lasing and Scattering	27
3.2 Basic Antenna Theory and HFSS Simulations	30
3.3 Antenna Modelization	34
4 Conclusion	43
A Bessel Functions	45
A.1 Definition and Elementary Properties	45
A.2 Asymptotic and Limiting Forms	47
B Basic Equations of Bidimensional Cavities	49
B.1 SALT Equations for TE and TM Polarizations	49
B.2 Specialization to Dielectric Cavities	49
C Numerical Tools	51

C.1	Numerical Computation of the Scattering Matrix	51
C.2	Computation of the Logarithmic Derivative $[H_{\nu}^{(\pm)}(z)]'/H_{\nu}^{(\pm)}(z)$	51
C.3	Wigner Symbols	56
C.4	Spherical Harmonics Transform	59
Bibliography		65
Index		69

List of Figures

1.1	Schematic representation of whispering-gallery modes	2
2.1	Schematic view of the reduction of Maxwell's equations from 3D to 2D	7
2.2	Geometry of a bidimensional cavity	10
2.3	Radial discretization for use in SQA	15
2.4	General form of absolute value of the Hankel matrix \mathcal{H}	19
2.5	Correspondance between the poles of the scattering matrix and the peaks of the time delay spectrum.	21
2.6	Mirror symmetry of the scattering matrix	21
2.7	Convergence properties of SQA when applied on the homogeneous disk	22
2.8	Delay spectrum and far-field.	23
2.9	Photon trajectories in a Gaussian deformation of the refractive index	25
3.1	Example of a 3-port network	35
3.2	S-parameters of the RF21 fibre design	35
3.3	Geometry of the fibre-antenna	37
3.4	AFM pictures of silver deposited onto glass plates	39
3.5	Thickness ratios as a function of the silver concentration	41
3.6	Experimental and simulated S_{11} parameter for the RF21 fibre	42
3.7	Pearson correlation coefficient as a function of the frequency shift of the data.	42
3.8	Fourier Power Spectrum	42
C.1	Maximum deviation between the CFE and Amos' implementation as a function of the CFE tolerance	55
C.2	Performance of the CFE compared to Amos' library's.	55
C.3	Performance and precision of our numerical algorithms.	59
C.4	Flowchart of the algorithm used to compute the coupling coefficients. SRHUGE is the square root of the biggest representable number in our floating point representation.	60
C.5	Precision of our implementation of the algorithm that evaluates the spherical harmonics	64

List of Tables

3.1	Units are repeated from column above if not indicated.	40
C.1	Parameters and coefficients of the three-term recursion relations satisfied by the $3j$ - and $6j$ -symbols. The expression $[++-]$ represents the coefficient $[j_1(j_1 + 1) + j_2(j_2 + 1) - j_3(j_3 + 1)]$ and similarly for other signs in the bracket.	61

*Dedicated to a special collection of
particles...*

education, *n.* That which discloses
to the wise and disguises from the
foolish their lack of understanding.

The Devil's Dictionary

Ambrose Bierce

Notation

Mathematical Operators

Symbol	Definition
$\mathbf{K}\left(\frac{a_m}{b_m}\right)$	Continued fraction expansion with coefficients a_m and b_m .
\sum_m	Sum over all angular momenta in two dimensions, $m = -\infty \dots \infty$.
$\sum_{\ell,m}$	Sum over all angular momenta in three dimensions, $\ell = 0 \dots \infty$, $m = -\ell \dots \ell$.
$\sum_{\sigma,\ell,m}$	Sum over all spinorial angular momenta in three dimensions.
$\lfloor x \rfloor$	Floor function. Maps x to the largest previous integer.
$\lceil x \rceil$	Ceiling function. Maps x to the smallest following integer.

Vectors and Matrices

Symbol	Definition
\mathbf{V}, \mathbf{v}	Vectors (bold and italic, uppercase and lowercase).
V_i, v_i	i th component of vector.
\mathbf{M}	Matrix (bold uppercase)
M_{ij}	Element on i th row and j th column. $(j + iN)$ th element of matrix (row-major ordering) where N is the number of columns. The indices start at 0.

Electromagnetism

Symbol	Definition
$\mathbf{E}, \mathbf{D}, \mathbf{P}$	Electric field, electric displacement and polarization.
$\mathbf{H}, \mathbf{B}, \mathbf{M}$	Magnetic field, magnetic induction and magnetization.
\mathbf{j}, ρ	Current and charge densities.
$\chi_{e,m}(\mathbf{r}, \mathbf{r}', t, t')$	Electric/magnetic tensorial susceptibility.
$\epsilon = \epsilon' + i\epsilon''$	Electric permittivity of a material. We often separate its real and imaginary parts as shown.
μ	Magnetic permeability of a material.
$n = \sqrt{\epsilon\mu}$	Refractive index of a material.
σ_e	Electric conductivity of a material.

Special Functions

Symbol	Definition
$J_\nu(z)$	Bessel function of the first kind of order ν .
$Y_\nu(z)$	Bessel function of the second kind of order ν .
$H_\nu^{(\pm)}(z), H_\nu^{(\omega)}(z)$	Hankel functions of the first and second kind, respectively, of order ν , $\omega = \pm$.
$U(a, b, z)$	Kummer's function, also known as the confluent hypergeometric function of the first kind, with parameters a, b .

Angular Momentum

Ordering of angular momentum in 2D. We consider both positive and angular momentum, so the matrices have size $2M + 1 \times 2M + 1$ where M is the maximum angular momentum.

$$\begin{array}{c}
 \begin{array}{c} - \\ \uparrow \\ - \\ \downarrow \\ + \end{array}
 \end{array}
 \begin{array}{c}
 \begin{array}{c} \leftarrow \\ \leftarrow \\ \leftarrow \\ \leftarrow \\ \leftarrow \end{array}
 \end{array}
 \begin{array}{c}
 \begin{array}{c} m' \\ 0 \end{array} \\
 \begin{array}{c} - \\ 0 \\ + \end{array}
 \end{array}
 \begin{array}{c}
 \begin{pmatrix}
 \ddots & & & \ddots \\
 & V_{-1-1} & V_{-10} & V_{-11} \\
 & V_{0-1} & V_{00} & V_{01} \\
 & V_{1-1} & V_{10} & V_{11} \\
 & \ddots & & \ddots
 \end{pmatrix}
 \begin{pmatrix}
 \vdots \\
 \psi_{-1} \\
 \psi_0 \\
 \psi_1 \\
 \vdots
 \end{pmatrix}
 \end{array}
 \end{array}
 \mathbf{V}\psi = m \begin{array}{c} \begin{array}{c} - \\ 0 \\ + \end{array} \end{array}$$

Ordering of angular momenta ℓ, m in 3D. This block structure allows the product

$$\sum_{\ell'=0}^{\infty} \sum_{m'=-\ell'}^{\ell'} V_{\ell m, \ell' m'} \psi_{\ell' m'}$$

to be written using a single index $\nu = (\ell, m)$. The matrices have size $(\ell_{\max} + 1)^2 \times (\ell_{\max} + 1)^2$.

$$\mathbf{V}\psi = \begin{matrix} \ell = 0 \\ \ell = 1 \end{matrix} \left\{ \begin{matrix} \overbrace{V_{00,00}}^{\ell' = 0} & \overbrace{V_{00,1-1} \quad V_{00,10} \quad V_{00,11}}^{m' = -\ell', \dots, \ell'} \\ V_{1-1,00} & V_{1-1,1-1} & \vdots & \vdots \\ V_{10,00} & \dots & \ddots & \vdots \\ V_{11,00} & \dots & \dots & \ddots \end{matrix} \right\} \begin{pmatrix} \psi_{00} \\ \psi_{1-1} \\ \psi_{10} \\ \psi_{11} \\ \vdots \end{pmatrix}$$

Glossary

Notation	Description	Page List
calibration phase (algorithms)	Wherein a numerical algorithm is tested against a problem with aknown solution. Oftentimes, convergence properties of the algorithm are determined using this (usually) trivial scenario.	20
Q-matrix	Time-delay matrix	5, 9, 13, 14
S-matrix	Scattering matrix	3, 5, 11, 14, 18, 20

Acronyms

ARC asymmetric resonant cavity. 3, 23

FEM finite element method. 4

LCX leaky coax antenna. 4

SALT steady-state *ab initio* laser theory. 4

SQA the **S**- and **Q**-matrix algorithm. 14, 15, 22

Preface

Physics, maze, lost in a maze, partial results

Contributions

This short section humbly presents my contribution to the literature in the form of both conference proceedings and peer-reviewed journal articles.

Peer-Reviewed Journal Articles

1. G. Painchaud-April[†], **J. Dumont**[†], D. Gagnon and L. J. Dubé, “Scattering method for resonances in dielectric microcavities,” *in preparation*.
2. D. Gagnon, **J. Dumont**, J.-L. Déziel and L. J. Dubé, “Ab initio investigation of lasing thresholds in photonic molecules,” *submitted for publication*. [arXiv:1401.7305](#).
3. D. Gagnon, **J. Dumont** and L. J. Dubé, “Multiobjective optimization in integrated photonics design,” *Opt. Lett* **38**, 2181–2184 (2013). [doi:10.1364/OL.38002181](#).
4. D. Gagnon, **J. Dumont** and L. J. Dubé, “Beam shaping using genetically optimized two-dimensional photonic crystals,” *J. Opt. Soc. Am. A* **29**, 2673–2678 (2012). [doi:10.1364/JOSAA.29.002673](#)

Conference Proceedings

1. D. Gagnon, **J. Dumont**, J.-L. Déziel and L. J. Dubé[‡], “Adding SALT to coupled microcavities: the making of active photonic molecule lasers,” in *IEEE Proceedings of the 16th International Conference on Transparent Optical Networks (ICTON 2014)*. [arXiv:1405.0168](#)
2. G. Painchaud-April, **J. Dumont**[§], D. Gagnon and L. J. Dubé, “S and Q matrices reloaded: applications to open, inhomogeneous, and complex cavities,” in *IEEE Proceedings of the 15th International Conference on Transparent Optical Networks (ICTON 2013)*. [doi:ICTON.2013.6602811](#).

[†]Both authors contributed equally to this work.

[‡]Speaker at this invited talk.

[§]Speaker at this invited talk.

3. D. Gagnon[†], **J. Dumont** and L. J. Dubé, “Coherent beam shaping using two-dimensional photonic crystals,” in IEEE Proceedings of the 15th International Conference on Transparent Optical Networks (ICTON 2013). [doi:ICTON.2013.6602751](https://doi.org/10.1109/ICTON.2013.6602751).

[†]Speaker at this regular talk.

Chapter 1

Introduction

Our story begins, as most stories do, with a simple premise. Circa 1878, John William Strutt, Third Baron Rayleigh – Lord Rayleigh, for short – observed a peculiar phenomena in St Paul’s Cathedral: a small whisper, uttered from one side of the circular gallery, could be heard quite clearly by anyone seated along the outer edge of the gallery and even travel back to the ears of the whisperer. To explain his observation, Lord Rayleigh borrowed from geometrical optics and modelled the sound waves as packets, or particles, of sound that undergo specular reflection upon contact with an obstacle [1, §287]. This picture, akin to the trajectories of billiard balls, allowed him to conclude that “sonorous vibrations have a tendency to cling to a concave surface”. The billiard analysis is later complemented by a complete wave analysis wherein he shows that the equation of aerial vibrations, essentially Helmholtz’s equation, admit solutions of the form

$$\psi_n(r, \theta, t) = J_n(kr) \cos(kat - n\theta)$$

and that most of the amplitude, for a certain range of parameters, is concentrated in an annulus near the boundary of the gallery [2], further proving his explanation. He also noted that his derivation held for electrical waves if the walls were perfectly conducting. He termed this phenomena the whispering-gallery phenomena and, today, we call this type of waves whispering-gallery waves.

Our story thus begins with the endless voyage of a whisper along a concave surface and all the secrets it may or may not convey..

1.1 The Study of Passive Dielectric Microcavities

For the better part of the 20th century, the whispering-gallery phenomena remained only a matter of curiosity [3]. It was brought back to light in the mid-1980s when it was realized that *dielectric resonators* had the potential to attain unparalleled electromagnetic energy storage capabilities via the use of whispering-gallery waves [4]. Research in this area exploded when their application

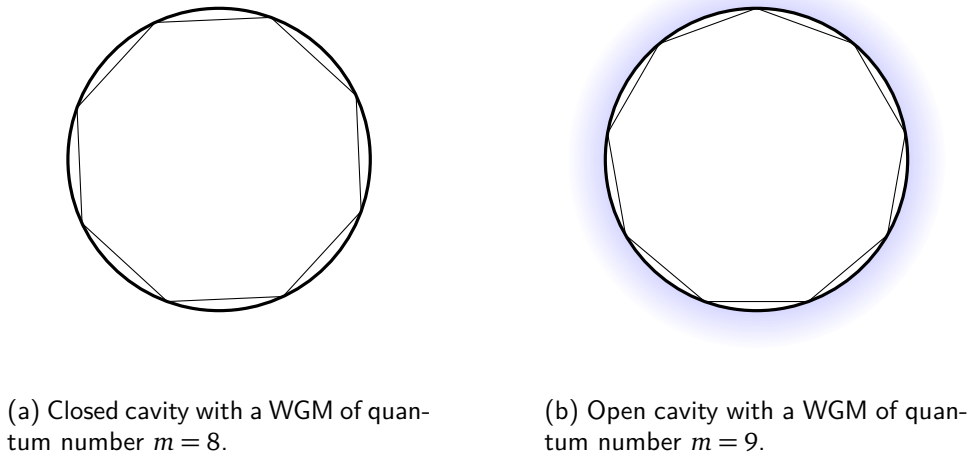


Figure 1.1 – Schematic representation of whispering-gallery modes in closed and open resonators. In closed resonators, WGMs have infinite lifetimes as they cannot interact with the external world. In open cavities, evanescent leakage (represented by the blue glow), implies finite modal lifetime.

as extremely sensitive biosensors was theoretically explored and later experimentally achieved [5–8].

The whispering-gallery phenomena in dielectric media can be explained via the same basic physics as the whispering gallery of St Paul’s Cathedral, but with a crucial difference: the mechanism by which the light (or sound) is confined. Both the cathedral and the metallic sphere described by Lord Rayleigh as known as *closed cavities*: the whisper does not leave the interior of the gallery as the electric field does not leave the confines of its metallic prison. The walls of the cavity do not allow the waves to penetrate their depth. On the other hand, dielectric cavities retain light by way of *total internal reflection*, which allows the wave to leak, or couple, to the exterior of the cavity. This has a slew of experimental and theoretical consequences.

Mathematically, closed cavities usually obey Helmholtz’s equation

$$[\nabla^2 + k^2]\psi = 0 \quad \psi(\mathbf{r} \in \mathcal{C}) = 0 \quad (1.1)$$

where ψ is the oscillation (pressure field, electric field, etc.) and \mathcal{C} is the boundary of the cavity. This partial differential equation together with the Dirichlet boundary condition translates to an eigenvalue problem: solutions only exist for a discrete set of eigenvalues k_n . These closed cavities have been a testbed for theoretical and experimental endeavours in the last three decades, as can be seen from the great amount of work done in the fields of quantum chaos and random matrix theory (RMT), for instance. Quantum chaos attempts to classify the chaotic eigenstates of systems with non-separable Schrödinger equations using the underlying (semi)classical mechanics of the cavity. Research in this area helps to define the classical-quantum transition. Level-spacing statistics of closed cavities also provides a way to classify the eigenstates, depending on the statistical ensemble the cavity describes.

Close cavities, are, however, an idealization of the much more realistic open cavity. The discrete states of the former exist indefinitely inside the cavity; they have an infinite lifetime. They thus have infinite energy storage capabilities, but are impossible to generate. The latter, which also obey Helmholtz equation, but with the Sommerfeld radiation condition (a Robin boundary condition)

$$\lim_{r \rightarrow \infty} r^{\frac{d-1}{2}} \left(\frac{\partial}{\partial r} - ik \right) \psi = 0 \quad (1.2)$$

have a continuum of solutions. These solutions have finite lifetimes. An incoming field from infinity can interact with the modes of the cavity and escape the confines of the cavity. The *time delay* introduced by the interaction is linked to the lifetime of the modes of the cavity.

This rather pictorial viewpoint can be made formal by the use of *scattering theory*, in which we suppose that a field, coming from infinity, suffers some changes due to its interaction with the cavity and escapes to infinity once again. The object that we will consider is the scattering matrix, which describes the relationship between the field after the interaction to the field before the interaction, i.e. it describes the effect of the potential on an incoming field. The scattering approach allows us to define the modes of open cavities, a problem that is perhaps more complicated than it seems (Fox-Li modes, modes of wave-chaotic...).

Open dielectric cavities also allow a semiclassical approximation, mathematically obtained by letting the wavelength λ to be very small compared to the characteristic lengths involved in the system, or $k \rightarrow \infty$. The resulting open billiard can and has been used to engineer the cavities to specific purposes. The fact that the resulting system is Hamiltonian (but not necessarily Hermitian) has been used to study open quantum systems and non-Hermitian quantum mechanics experimentally. This stems from the similarities between the Helmholtz and Schrödinger equations.

Most applications of open dielectric cavities urge the use of very high Q resonances. In WGM biosensors, the Q value dictates the performance of the sensor; in microlasers, it means a better field enhancement; in cavity QED, higher Q and lower mode volumes make it possible to study the quantum effects of light-matter interaction. It is possible to experimentally obtain values of $Q \sim 10^7 - 10^9$ using highly symmetrical cavity designs. This symmetry implies that the far-field emission is also symmetry: it usually is isotropic. For some applications, such as some designs of WGM biosensors, this may be fine. However, for lasing applications, one would like to have, simultaneously, high- Q and directionality in the far-field emission. The duality of those two concepts is one of the many facets of the study of asymmetric resonant cavities (ARCs), dielectric cavities that are parametrically deformed versions of the circular cavity. This allows a certain degree of freedom in the design of microcavities and has led to interesting phenomena, such as ...

In this thesis, we will add a second degree of freedom in the design by allowing the refractive index distribution to be completely arbitrary inside the cavity. This new degree of freedom can be realized experimentally by the use of nematics. Moreover, we will see that the numerical methods

Discuss
reso-
nances
and Q
values.

Discuss
CAT,
biosens-
ing,
micro-
lasers...

Add refer-
ences.

add refer-
ences.

developed in this context could also be used to better model the lasing operation of active dielectric cavities.

1.2 Onwards to Radiating Structures

The expertise developed in the study of dielectric cavities was later extended to lasing cavities and proposed for arbitrary 3D structures. We will touch upon the modelization of active dielectric cavities with the use of steady-state *ab initio* laser theory (SALT) which, as its name hints, provides a steady-state model for the behaviour of the active medium. The particular set of approximations used allow to model the population dynamics of quantum N -level systems as a static, but possibly spatially-varying and non-linear, modification of the refractive index of the passive cavity. In the linear case, basis expansions methods (such as the ones we use) can be applied. We will consider another numerical approach that has the potential to better compute the interior field, the variable phase method.

We will also discuss the application of the method to arbitrary 3D structures. We will attempt to model a type of antennae called leaky coax antenna (LCX). Their highly non-trivial geometry and the specifics of their experimental realization will make our method rather hard to implement in that case. We will thus use all-numerical methods to extract the necessary information. Proper introduction to this project will be given later.

1.3 Content of this Work

In first chapter of this thesis, we detail our work on open dielectric cavities with arbitrary refractive index profiles. We generalize a scattering method by G.P.-A. [9] for complex refractive indices and TE polarization. We first describe the analytical formalism and develop some of the scattering theory that is needed. We then discuss the development and numerical implementation of the solution of Helmholtz's equation in inhomogeneous cavities. We then showcase the method by analyzing a circular microcavity with a Gaussian deformation of its refractive index.

The second chapter discuss the extension to lasing structures and briefly discusses the variable phase method. We then model a family of LCXs with the finite element method (FEM). Most of the work done aimed to reconcile the experimental and theoretical data sets, mainly by explaining the source of the discrepancy. The effects of several physical parameters were thus explored.

Chapter 2

Passive Media

This chapter is devoted to the study of light propagation in dielectric bidimensional cavities. Starting from Maxwell's equations, we derive approximate differential equations that govern the wave behaviour in cavities having spatially-varying refractive index profiles (henceforth referred to as *inhomogeneous cavities*). This set of reduced equations serves as the basis for a semi-analytical solution method that uses the quantum machinery of the \mathbf{S} -matrix and its associated time-delay matrix to yield information about the cavity modes. The numerical implementation of the method is discussed and is then demonstrated for a selected set of microcavities.

2.1 Maxwell's Equations for Bidimensional Cavities: Reduction from 3D to 2D

2.1.1 Setting the Stage

As with any problem in optics, we start from Maxwell's equations. Although this specific chapter focuses on dielectric cavities, we will show Maxwell's equations in their full generality, as we will later study problems with currents and sources. We use the Lorentz-Heaviside set of units with the speed of light, c , equal to 1.

$$\nabla \times \mathbf{E}(\mathbf{r}, t) + \frac{\partial \mathbf{B}(\mathbf{r}, t)}{\partial t} = 0 \quad (2.1a)$$

$$\nabla \times \mathbf{H}(\mathbf{r}, t) - \frac{\partial \mathbf{D}(\mathbf{r}, t)}{\partial t} = \mathbf{j}_s(\mathbf{r}, t) + \mathbf{j}_c(\mathbf{r}, t) \quad (2.1b)$$

$$\nabla \cdot \mathbf{D}(\mathbf{r}, t) = \rho(\mathbf{r}, t) \quad (2.1c)$$

$$\nabla \cdot \mathbf{B}(\mathbf{r}, t) = 0 \quad (2.1d)$$

where \mathbf{E} is the electric field, \mathbf{D} the electric displacement, \mathbf{H} the magnetic field, \mathbf{B} the magnetic induction and where \mathbf{j} and ρ are the current and charge densities, respectively. The distinction between a source current, \mathbf{j}_s and an induced conduction current, \mathbf{j}_c , is arbitrary but will prove

conceptually useful when dealing with radiating structures (see next chapter). In this thesis, we will generally take $\rho = 0$ and $\mathbf{j}_s = \mathbf{0}$ as there will be no physical charges/currents in our problems.

This very general set of equations does not make any assumption on the properties of the medium in which the fields exist: it is, therefore, almost impossible to solve. To properly model the effect of different media, we introduce the usual constitutive relations:

$$\mathbf{D}(\mathbf{r}, t) = \mathbf{E}(\mathbf{r}, t) + \mathbf{P}(\mathbf{r}, t) \quad (2.2a)$$

$$\mathbf{B}(\mathbf{r}, t) = \mathbf{H}(\mathbf{r}, t) + \mathbf{M}(\mathbf{r}, t) \quad (2.2b)$$

where the effects of the medium are accounted for in \mathbf{P} and \mathbf{M} , the polarization and magnetization fields, respectively. In the time domain, the effect of the electric (magnetic) field on the polarization (magnetization) can be written as

$$\mathbf{P} = \iiint \chi_e(\mathbf{r}, \mathbf{r}', t, t'; \mathbf{E}) \cdot \mathbf{E}(\mathbf{r}', t') d^3 \mathbf{r}' dt' + \mathbf{P}^{NL} \quad (2.3a)$$

$$\mathbf{j}_c = \iiint \sigma_e(\mathbf{r}, \mathbf{r}', t, t'; \mathbf{E}) \cdot \mathbf{E}(\mathbf{r}', t') d^3 \mathbf{r}' dt' + \mathbf{j}_c^{NL} \quad (2.3b)$$

$$\mathbf{M} = \iiint \chi_m(\mathbf{r}, \mathbf{r}', t, t'; \mathbf{H}) \cdot \mathbf{H}(\mathbf{r}', t') d^3 \mathbf{r}' dt' + \mathbf{M}^{NL} \quad (2.3c)$$

where $\chi_{e,m}$ are the electric and magnetic tensorial susceptibilities and σ_e the tensorial electric conductivity. They are written here as (possibly non-linear) response functions. We will take the nonlinear magnetization and induced current, \mathbf{M}^{NL} and \mathbf{j}_c^{NL} , to be identically zero. While \mathbf{P}^{NL} is usually reserved for the nonlinear polarization, we will use it to denote the effect of a gain medium, whether it is nonlinear or not.

While it is possible to compute these quantities from first principles using statistical mechanics techniques, this is a highly complicated topic that we will not delve into. We will consider local, causal and isotropic (although possibly spatially varying) responses. The tensorial response functions become scalar and their spatial dependence is given by a three dimensional Dirac δ -function. This allows us to write the constitutive relations in the much simpler form

$$\mathbf{P} = \int_0^\infty \chi_e(\mathbf{r}, t') \mathbf{E}(\mathbf{r}, t - t') dt' + \mathbf{P}^{NL} \quad (2.4a)$$

$$\mathbf{j}_c = \int_0^\infty \sigma_e(\mathbf{r}, t') \mathbf{E}(\mathbf{r}, t - t') dt' \quad (2.4b)$$

$$\mathbf{M} = \int_0^\infty \chi_m(\mathbf{r}, t') \mathbf{H}(\mathbf{r}, t - t') dt' \quad (2.4c)$$

Substituting these results into the Maxwell equations and using the Fourier transform yields

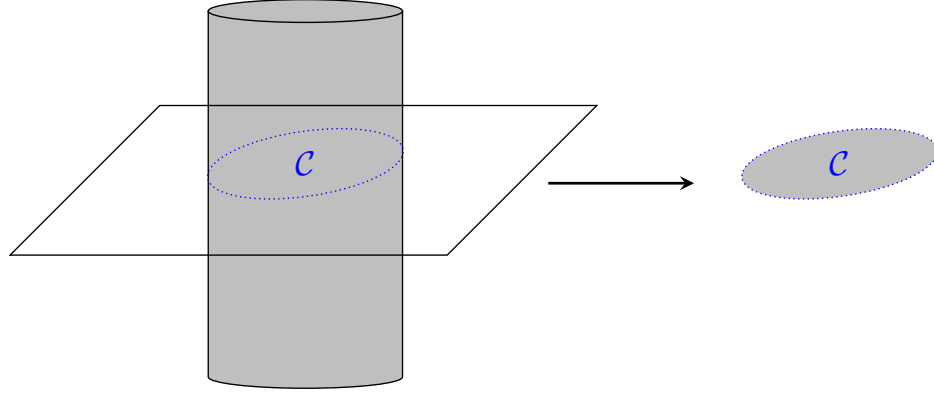


Figure 2.1 – Our set of equations will be valid for infinitely long cylinders of arbitrary cross-sections (shown on the left) and arbitrary physical parameters ϵ and μ . Our cavities, however, are bidimensional (shown on the right). The dimension reduction thus consists in postulating independence of the fields and physical and geometrical parameters of the cavity with regards to the longitudinal coordinate and choosing a particular plane $\partial\Omega$.

the set

$$\nabla \times \mathbf{E}(\mathbf{r}, \omega) - i\omega\mu(\mathbf{r}, \omega)\mathbf{H}(\mathbf{r}, \omega) = 0 \quad (2.5a)$$

$$\nabla \times \mathbf{H}(\mathbf{r}, \omega) + i\omega\epsilon(\mathbf{r}, \omega)\mathbf{E}(\mathbf{r}, \omega) = -i\omega\mathbf{P}^{NL}(\mathbf{r}, \omega) \quad (2.5b)$$

where $\mu = 1 + \chi_m$ is the permeability and $\epsilon = 1 + \chi_e - \sigma/i\omega$ the permittivity. In the remainder of this thesis, we will be concerned by the solution of this precise set of equations. We also recall the *electromagnetic boundary conditions* associated with a discontinuous jump in the permeability or permittivity

$$\hat{\mathbf{n}} \cdot (\mathbf{B}_2 - \mathbf{B}_1) = 0, \quad \hat{\mathbf{n}} \times (\mathbf{E}_2 - \mathbf{E}_1) = 0, \quad (2.5c)$$

$$\hat{\mathbf{n}} \times (\mathbf{H}_2 - \mathbf{H}_1) = \mathbf{K}, \quad \hat{\mathbf{n}} \cdot (\mathbf{D}_2 - \mathbf{D}_1) = \Sigma. \quad (2.5d)$$

2.1.2 Dimension Reduction

In this section we derive the differential equations for the electromagnetic field in an infinitely long dielectric cylinder of arbitrary cross-section and arbitrary physical parameters ϵ and μ . There is no gain medium. Consequently, $\mathbf{P}^{NL} = \mathbf{K} = \Sigma \equiv 0$ in our previous equations. We also require translational symmetry, i.e. that there exist no parametric dependence on z .

To this effect, it will be useful to separate the field in transverse and longitudinal components. Following [10, 11], we suppose the fields can be written as

$$\begin{Bmatrix} \mathbf{E}(\mathbf{r}_\perp, z) \\ \mathbf{H}(\mathbf{r}_\perp, z) \end{Bmatrix} = \begin{Bmatrix} \mathbf{E}(\mathbf{r}_\perp) \\ \mathbf{H}(\mathbf{r}_\perp) \end{Bmatrix} e^{i\beta z} \quad (2.6)$$

Notice that, in our system of units, $\omega = k$ and thus we will make use of frequency and wavenumber interchangeably. We will also suppress all explicit frequency dependence from our notation, as it rapidly becomes cumbersome.

and we will also separate the fields and differential operators in two parts

$$\mathbf{E}(\mathbf{r}_\perp) = \mathbf{E}_\perp + E_z \hat{\mathbf{z}}; \quad \nabla = \nabla_\perp + \hat{\mathbf{z}} \frac{d}{dz}. \quad (2.7)$$

Substitution in (2.5a) yields

$$ik\mu H_z = (\nabla_\perp \times \mathbf{E}_\perp)_z \quad -ik\epsilon E_z = (\nabla_\perp \times \mathbf{H}_\perp)_z \quad (2.8)$$

$$ik\mu \mathbf{H}_\perp = (-i\beta \mathbf{E}_\perp + \nabla_\perp E_z) \times \hat{\mathbf{z}} \quad -ik\epsilon \mathbf{E}_\perp = (-i\beta \mathbf{H}_\perp + \nabla_\perp H_z) \times \hat{\mathbf{z}} \quad (2.9)$$

The symmetry of these equations allow the decoupling of the tranverse and longitudinal components. Solving the system (2.9) shows that the scalar components H_z and E_z are the fundamental ones:

$$\mathbf{E}_\perp = \frac{i}{k^2 n^2 - \beta^2} [\beta \nabla_\perp E_z + k\mu \nabla_\perp H_z \times \hat{\mathbf{z}}] \quad (2.10a)$$

$$\mathbf{H}_\perp = \frac{i}{k^2 n^2 - \beta^2} [-k\epsilon \nabla_\perp E_z \times \hat{\mathbf{z}} + \beta \nabla_\perp H_z]. \quad (2.10b)$$

Derivation of the differential equation for E_z and H_z can be done via equations (2.8), but is quite cumbersome. A component-wise approach is thus presented in Appendix B.

More specific boundary conditions can be derived with the use of these equations. Applying the tranverse and longitudinal decomposition on (2.5c) yields the six boundary conditions

$$\begin{aligned} E_{z1} &= E_{z2} & H_{z1} &= H_{z2} \\ E_{t1} &= E_{t2} & H_{t1} &= H_{t2} \\ \epsilon_1 E_{n1} &= \epsilon_2 E_{n2} & \mu_1 H_{n1} &= \mu_2 H_{n2} \end{aligned}$$

We seek to write the boundary conditions as a function of H_z and E_z , given that they are the fundamental fields. This can be done by taking the projections of the tranverse fields:

$$E_t = \hat{\mathbf{t}} \cdot \mathbf{E}_\perp = \frac{i}{\gamma^2} [\beta \partial_t E_z - k\mu \partial_n H_z] \quad (2.11a)$$

$$E_n = \hat{\mathbf{n}} \cdot \mathbf{E}_\perp = \frac{i}{\gamma^2} [\beta \partial_n E_z + k\mu \partial_t H_z] \quad (2.11b)$$

$$H_t = \hat{\mathbf{t}} \cdot \mathbf{H}_\perp = \frac{i}{\gamma^2} [k\epsilon \partial_n E_z + \beta \partial_t H_z] \quad (2.11c)$$

$$H_n = \hat{\mathbf{n}} \cdot \mathbf{H}_\perp = \frac{i}{\gamma^2} [-k\epsilon \partial_t E_z + \beta \partial_n H_z] \quad (2.11d)$$

where $\partial_{t,n}$ are the tranverse and normal derivatives, respectively, and $\gamma^2 = k^2 n^2 - \beta^2$. Substituting these results in the boundary conditions for the tranverse and normal components, we can derive the conditions $\partial_t E_{z1} = \partial_t E_{z2}$, $\partial_t H_{z1} = \partial_t H_{z2}$, which can shown to be equivalent to the continuity of the longitudinal components, viz. (2.11a) [11]. Combining all our previous results yields the

four independent boundary conditions:

$$E_{z1} = E_{z2} \quad (2.12a)$$

$$H_{z1} = H_{z2} \quad (2.12b)$$

$$\frac{k\mu_1}{\gamma_1^2} \frac{\partial H_{z1}}{\partial n} - \frac{k\mu_2}{\gamma_2^2} \frac{\partial H_{z2}}{\partial n} = \beta \left(\frac{1}{\gamma_1^2} - \frac{1}{\gamma_2^2} \right) \frac{\partial E_{z1}}{\partial t} \quad (2.12c)$$

$$\frac{k\epsilon_1}{\gamma_1^2} \frac{\partial E_{z1}}{\partial n} - \frac{k\epsilon_2}{\gamma_2^2} \frac{\partial E_{z2}}{\partial n} = -\beta \left(\frac{1}{\gamma_1^2} - \frac{1}{\gamma_2^2} \right) \frac{\partial H_{z1}}{\partial t}. \quad (2.12d)$$

Notice that the propagation constant couples the electric and magnetic field, regardless of the physical and geometrical parameters of the cavity.

2.2 Scattering Matrix Formalism

The previous section has provided us with the differential equations that we will need to solve to properly model bidimensional cavities. In this section, we will set up a scattering matrix (**S**-matrix) formalism, augmented by the **Q**-matrix that will allow us to quantify the response of the cavities to an applied field and provide us with a novel way to determine their resonances. The numerical implementation of the method, being somewhat problematic, will be discussed at length.

2.2.1 **S** and **Q** Matrices Reloaded

In dielectric cavities, we need to solve the following equations

$$\begin{aligned} \left\{ \nabla^2 + k^2 n^2 \left[1 - \left(\frac{\beta}{kn} \right)^2 \right] \right\} \begin{Bmatrix} H_z \\ E_z \end{Bmatrix} &= \frac{1}{1 - \left(\frac{\beta}{kn} \right)^2} \left[\frac{1}{\epsilon} \begin{Bmatrix} \nabla H_z \\ \nabla E_z \end{Bmatrix} \cdot \nabla \epsilon + \frac{1}{\mu} \begin{Bmatrix} \nabla H_z \\ \nabla E_z \end{Bmatrix} \cdot \nabla \mu \right] \\ &- \begin{pmatrix} \frac{1}{\mu} & 0 \\ 0 & \frac{1}{\epsilon} \end{pmatrix} \begin{Bmatrix} \nabla H_z \cdot \nabla \mu \\ \nabla E_z \cdot \nabla \epsilon \end{Bmatrix} + \frac{\beta/kn}{1 - \left(\frac{\beta}{kn} \right)^2} \left[\left(\sqrt{\frac{\mu}{\epsilon}} + \sqrt{\frac{\epsilon}{\mu}} \right) \begin{pmatrix} 0 & -\frac{1}{\mu} \\ \frac{1}{\epsilon} & 0 \end{pmatrix} \begin{Bmatrix} \nabla H_z \times \nabla \mu \\ \nabla E_z \times \nabla \epsilon \end{Bmatrix} \right] \end{aligned} \quad (2.13)$$

where β is the propagation constant in the longitudinal direction. Inhomogeneous cavities do not obey Helmholtz's equation like homogeneous cavities do, but depend upon the first-order derivatives of the fields and physical properties of the medium. The two longitudinal fields couple through the last term, where an antidiagonal matrix appears.

In fact, this set of equations describe the propagation of light in optical fibers of arbitrary cross-section and arbitrary refractive index profiles. However, we are interested in the modes that are confined on a two-dimensional surface, the cavity modes. These modes must be independent of z and we therefore take $\beta = 0$. This is the main approximation of our model. It has been shown to hold only approximately in experimental conditions [12, 13], but we take the resulting equations to be the exact one. This allow a simpler analysis for qualitative exploration; quantitative agreement could be reached via perturbation methods. This approximation has the much appreciated benefit of decoupling both the field equations and the boundary conditions (see (2.12)).

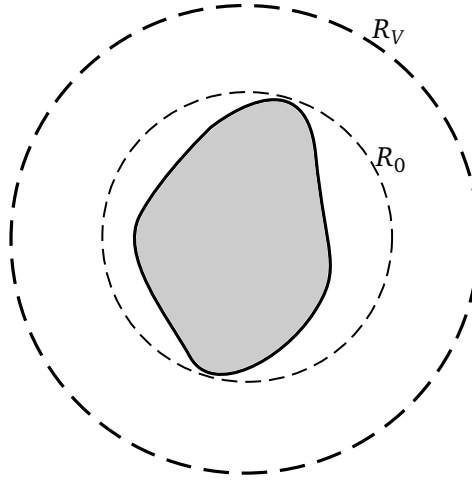


Figure 2.2 – Geometry of a dimensional cavity. R_0 is the radius of the smallest circle that encloses the physical microcavity. R_V is the radius of a fictional circle that we will take to go to infinity.

Additionally exploiting the fact that we will only consider non-magnetic media ($\mu = 1$, $\epsilon = n^2$), our equation set becomes

$$[\nabla^2 + k^2 n^2] H_z = \frac{2}{n} \nabla H_z \cdot \nabla n \quad (2.14a)$$

$$[\nabla^2 + k^2 n^2] E_z = 0. \quad (2.14b)$$

In the following, it will be advantageous to form the field $\mathbf{h} = \mathbf{H}/n$ [14]. This yields the equation [9, 14]

$$\left[\nabla^2 + k^2 n^2 - \frac{2(\nabla n)^2}{n^2} + \frac{(\nabla^2 n)}{n} \right] h_z = 0 \quad (2.14a')$$

which is nothing but Helmholtz equation with an additional potential term.

To solve these equations, we will adopt a scattering viewpoint. Imagine that the dielectric cavity is embedded in an infinite medium of constant refractive index $n_o = \sqrt{\epsilon\mu}$, outside the cavity, $\mathbf{r} \notin \mathcal{C}$, the r.h.s. of our set vanishes. The resulting equations are Helmholtz's and therefore have the well-known solution

$$\psi = \sum_m [A_m H_m^{(-)}(nkr) + B_m H_m^{(+)}(nkr)] e^{im\theta} \quad (r > R_0). \quad (2.15)$$

where $H_m^{(\pm)}(z)$ are the Hankel functions of the first and second kind. The Hankel functions are chosen in lieu of their usual homologues $J_m(z)$ and $Y_m(z)$ as their asymptotic forms have incoming/outgoing cylindrical wave character, $H_m^{(\pm)} \propto \exp(\pm ikr)/\sqrt{r}$. The scattering viewpoint essentially describes the relationship between the outgoing coefficients, B_m , and the incoming coefficients, A_m via the *scattering matrix*

$$B_m = S_{mm'} A_{m'}. \quad (2.16)$$

Much like its quantum-mechanical counterpart, the scattering matrix can be interpreted as a phase shift acquired by the incoming waves through interaction with the potential. This is most easily seen by considering a central potential $V(r)$ where the \mathbf{S} -matrix is diagonal. In that case, the m component of the field can be written as

$$\psi_m \propto \frac{1}{\sqrt{r}} [e^{-ikr} + e^{i\delta_m} e^{ikr}] \quad (2.17)$$

where we have written $S_{mm} = e^{i\delta_m}$ with $\delta_m \in \mathbb{R}$ as per the unitarity condition. The non-diagonal generalization $S_{mm'}$ describes the coupling between angular momenta $m \rightarrow m'$ and can be interpreted as a transition probability. It should be noted that the \mathbf{S} -matrix contains all near- and far-field information.

In most applications, we wish to find the *resonances* of the cavity. This is usually done by enforcing Sommerfeld radiation conditions on Helmholtz's equation and looking for solutions of

link to introduction

$$\mathbf{S}^{-1} \mathbf{B} = 0; \quad (2.18)$$

i.e. an infinitesimal input provides an infinite output. A solution exists only if $|\det \mathbf{S}(k)| \rightarrow \infty$, at a pole of the \mathbf{S} -matrix. For real potentials, there cannot exist a solution on the real k line because of the flux conservation (unitarity) property of the \mathbf{S} -matrix. We must extend the search to the complex k plane.

Non-renormalizable QB states.

Complex potentials -> trajectory of poles in k plane to real line. Freddy foreshadowing for next part.

We will proceed a different way. It is possible to find the signatures of these poles on the real k line by computing the *energy* of the modes and their complex coupling. This part of the formalism was initially developed by G.P.-A. [9]: we will repeat only what is necessary.

Recall that the average electromagnetic energy of a field in a given volume V

$$\mathcal{E}^V = \frac{1}{2} \iiint_V [\epsilon \mathbf{E}^* \cdot \mathbf{E} + \mu \mathbf{H}^* \cdot \mathbf{H}] d^3 \mathbf{r}. \quad (2.19)$$

We form the energy matrix

$$\mathcal{E}_{mm'}^V = \frac{1}{2} \iiint_V [\epsilon \mathbf{E}_m^* \cdot \mathbf{E}_{m'} + \mu \mathbf{H}_m^* \cdot \mathbf{H}_{m'}] d^3 \mathbf{r}. \quad (2.20)$$

We will carry out the rest of the computation for the TM mode ($H_z = E_r = E_\theta = 0$); the argument holds for TE polarisation *mutatis mutandis* because of the k -independence of the additional

potential term in (2.14a') and also because $\mathbf{h} \propto \mathbf{H}$ for $r > R_0$. We thus have

$$\begin{aligned} \mathbf{E} &= \psi \hat{\mathbf{z}} \\ \mathbf{H} &= \frac{1}{ik} \nabla \times \mathbf{E} \end{aligned}$$

and the energy matrix becomes

$$\mathcal{E}_{mm'}^V = \frac{1}{2} \iiint_V \left[\epsilon \psi_m^* \psi_{m'} + \frac{1}{k^2} (\nabla \times \psi_m \hat{\mathbf{z}}) \cdot (\nabla \times \psi_{m'}^* \hat{\mathbf{z}}) \right] d^3 \mathbf{r}. \quad (2.21)$$

Taking the parametric derivative of Helmholtz' equation, we get the following relations

$$[\nabla^2 + n^2 k^2] \psi = 0 \quad (2.22a)$$

$$[\nabla^2 + n^2 k^2] \psi^* = 0 \quad (2.22b)$$

$$\nabla^2 \frac{\partial \psi}{\partial k} + 2kn^2 \psi + n^2 k^2 \frac{\partial \psi}{\partial k} = 0 \quad (2.22c)$$

where we assume a real potential. Forming the product

$$\begin{aligned} \frac{1}{2k} \nabla \cdot \left[\frac{\partial \psi}{\partial k} \nabla \psi^* - \psi^* \nabla \frac{\partial \psi}{\partial k} \right] &= \frac{1}{2k} \left[\nabla \psi^* \cdot \nabla \frac{\partial \psi}{\partial k} + \frac{\partial \psi}{\partial k} \nabla^2 \psi^* - \nabla \frac{\partial \psi}{\partial k} \cdot \nabla \psi^* - \psi^* \nabla^2 \frac{\partial \psi}{\partial k} \right] \\ &= \frac{1}{2k} \left[n^2 \psi^* \left(2k\psi + k^2 \frac{\partial \psi}{\partial k} \right) - \frac{\partial \psi}{\partial k} n^2 k^2 \psi^* \right] \\ &= n^2 \psi^* \psi \end{aligned}$$

where we have used the identity [15, Appendix II]

$$\nabla \cdot (\phi \mathbf{A}) = \mathbf{A} \cdot \nabla \phi + \phi \nabla \cdot \mathbf{A}. \quad (2.23)$$

We will also use the identity

$$(\mathbf{a} \times \mathbf{b}) \cdot (\mathbf{c} \times \mathbf{d}) = \mathbf{a} \cdot [\mathbf{b} \times (\mathbf{c} \times \mathbf{d})] \quad (2.24)$$

to write the energy matrix as

$$\mathcal{E}_{mm'}^V = \frac{1}{4k} \int_V \nabla \cdot \left\{ \frac{\partial \psi_{m'}}{\partial k} \nabla \psi_m^* - \psi_m^* \nabla \frac{\partial \psi_{m'}}{\partial k} + \frac{2}{k} [\psi_{m'} \hat{\mathbf{z}} \times \nabla \times \psi_m^* \hat{\mathbf{z}}] \right\} d^3 \mathbf{r} \quad (2.25)$$

Using the divergence theorem, noting that the normal vector is the radial vector, we obtain

$$\mathcal{E}_{mm'}^V = \frac{wR_V}{4k} \int_0^{2\pi} \left(\frac{\partial \psi_{m'}}{\partial k} \frac{\partial \psi_m^*}{\partial r} - \psi_m^* \frac{\partial^2 \psi_{m'}}{\partial k \partial r} \right) d\theta + \frac{wR_V}{2k} \int_0^{2\pi} \psi_{m'} \frac{\partial \psi_m^*}{\partial r} d\theta$$

Using the exterior solution for ψ_m and using the asymptotic expressions (A.16c) for the Hankel functions, we get (after some algebra)

$$\mathcal{E}_{mm'}^\infty = \lim_{R_V \rightarrow \infty} \left[\frac{4n_0 w R_V}{k} + \mathcal{O}(R_V^{-1}) \right] \delta_{mm'} + \frac{4w}{k} \left(-i \sum_\ell S_{\ell m}^* \frac{\partial S_{\ell m'}}{\partial k} \right) \quad (2.26)$$

where w is the thickness of the cavity. The first term is the diverging energy of the beam. Given that the incoming and outgoing waves are of infinite extent, this divergence is only natural. The second term, however, depends only the potential and can be interpreted as an excess energy due to the cavity [9]. In matrix notation, we have

$$\mathbf{Q} = -i\mathbf{S}^\dagger \frac{d\mathbf{S}}{dk}. \quad (2.27)$$

This result coincides with the \mathbf{Q} -matrix of quantum mechanics [16]. The interpretation of this matrix is facilitated by (2.17). Using the central potential, we can write

$$Q_{mm} = -ie^{-i\delta_m} \left(i \frac{\partial \delta_m}{\partial k} \right) e^{i\delta_m} = \frac{\partial \delta_m}{\partial k}. \quad (2.28)$$

The \mathbf{Q} -matrix thus corresponds to the energy derivative of the phase shift, which has long been associated with the time-delay introduced by the potential [16–18].

The keen reader will have noticed that the above derivation fails for complex potentials. The author has not found a proper derivation for the extension to complex potentials. However, an expression can be found by this heuristic argument: when the potential is complex, the phase shift δ_m becomes a complex function of k . In the preceding expression, we should take the inverse of the scattering matrix, not its Hermitian transpose, to reproduce the energy derivative of the phase shift. We thus have

$$\mathbf{Q} = -i\mathbf{S}^{-1} \frac{\partial \mathbf{S}}{\partial k} \quad (2.29)$$

as the proper generalization. This form was also used by Smith in [16].

2.2.2 Properties of the \mathbf{S} and \mathbf{Q} matrices

The \mathbf{S} -matrix has multiple symmetries which can be used either to verify numerical implementations or to help tame numerical divergence issues. Most of the symmetries we will expose in this thesis will concern the analytical continuation of the scattering matrix in the complex k plane.

It is well known that the \mathbf{S} -matrix is unitary for real values of n and k [19]. However, it loses this important property is lost when we extend to the complex plane. Looking at the complex conjugated versions of our equation set, we see that we have

$$\begin{aligned} B_m &= S_{mm'}(n, k) A_{m'} \\ A_m^* &= S_{mm'}(n^*, k^*) B_{m'}^* \end{aligned}$$

we can obtain the relation

$$\mathbf{S}^{-1}(n^*, k^*) = \mathbf{S}^\dagger(n, k) \quad (2.30)$$

which reduces to the unitarity condition when the values are real.

Following [9], we set up the following scattering “experiment”:

$$H_m^{(-)}(z)e^{im\theta} \rightarrow \sum_{m'} S_{m'm}(n, k) H_{m'}^{(+)}(z)e^{im'\theta} \quad (\text{initial reaction})$$

$$\sum_m S_{m'm}^*(n^*, k^*) H_m^{(-)}(z)e^{im\theta} \rightarrow H_{m'}^{(+)}(z)e^{im'\theta} \quad (\text{relation (2.30)})$$

$$\sum_m S_{m'm}(n^*, k^*) \overline{H_m^{(-)}(z)e^{-im\theta}} \leftarrow \overline{H_{m'}^{(+)}(z)e^{-im'\theta}}. \quad (\text{complex conjugate (time reversal)})$$

Use of (A.8c) leads to the relation, valid only when $k \in \mathbb{R}$

$$S_{m'm}(n, k) = (-1)^{m'} S_{-m-m'}(n^*, k)(-1)^m. \quad (2.31)$$

This relationship will be incredibly useful in the numerical implementation.

The \mathbf{Q} -matrix also has some interesting properties. For real potentials, it is Hermitian. This is a direct consequence of the unitarity of the \mathbf{S} -matrix as

$$\frac{d\mathbf{S}^\dagger \mathbf{S}}{dk} = \frac{d\mathbf{S}^\dagger}{dk} \mathbf{S} + \mathbf{S}^\dagger \frac{d\mathbf{S}}{dk} = 0 \quad (2.32)$$

and

$$\mathbf{Q}^\dagger = i \frac{d\mathbf{S}^\dagger}{dk} \mathbf{S} = -i \mathbf{S}^\dagger \frac{d\mathbf{S}}{dk} = \mathbf{Q} \quad (2.33)$$

The delays associated with the potential are thus always real and the delay eigenstates form a complete basis.

Lorentzian form of the delay.

In the complex case, the phase shifts become complex, as do the time delays. The imaginary part can be interpreted as an emission/absorption time scale.

2.3 Numerical Implementation

The numerical computation of the scattering matrix depends on two constructs: a polar discretization scheme and interior scattering matrices. We choose, for the former, a rather standard radial discretization (see Fig. 2.3). For easier reference, we dub the method the \mathbf{S} - and \mathbf{Q} -matrix algorithm (SQA).

The latter relate the solutions of the differential equation inside each radial shell to its neighboring shell. The final interior scattering matrix relates the solution in the last shell to the exterior solution, which is analytically known and is related to the \mathbf{S} -matrix of the cavity.

Our method is based on an algorithm originally developed by Rahachou and Zozoulenko [20] and extended by [9]. We generalize the method to accept complex refractive index profiles n and wavenumbers k .

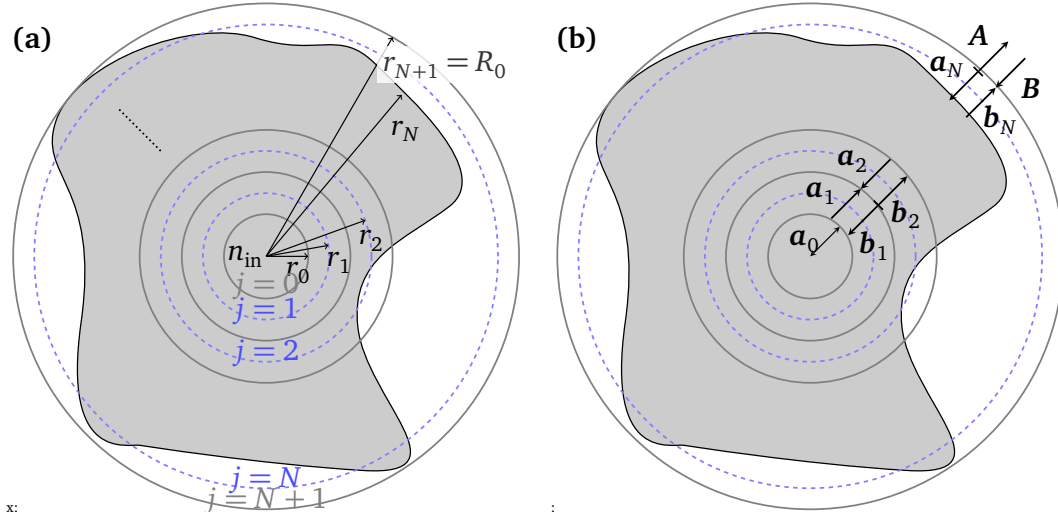


Figure 2.3 – Radial discretization of the cavity for use in SQA. The inner circle is assumed to have a constant refractive index denoted n_{in} . The full grey lines represent the physical boundaries of each shell while the dotted blue lines represent their center.

2.3.1 Divide et impera

We wish to solve the Helmholtz equation

$$[\nabla^2 + k^2 n^2] \psi = 0 \quad (2.34)$$

inside the cavity. For $r > R_0$, the radius of the smallest circle that encloses the whole dielectric, the solution is (2.15). We apply the discretization of Fig. 2.3. We define a set of radii $\{r_j\}_{j=0}^{N+1}$ that denote the positions of the center of the different shells. As such, $r_j - r_{j-1} = 2\epsilon$ for the inner shells. The cases $j = 0$ and $j = N + 1$ are different in that r_0 and r_{N+1} denote the outer and inner limits of the domains, respectively. Moreover, $r_{N+1} - r_N = r_1 - r_0 = \epsilon \neq 2\epsilon$. As our first approximation, we suppose that the refractive index inside the inner circle is constant and call it n_{in} . The Helmholtz equation then merely becomes the Bessel equation (A.1). Enforcing finiteness of the field at $r = 0$, we have the solution

$$|\psi(r)\rangle = \sum_m 2a_m^0 J_m(n_{\text{in}}kr) |\Phi_m^0\rangle \quad (r < r_0) \quad (2.35)$$

where we have introduced bra-ket notation for the angular part of the solution. In that case,

$$\langle \theta | \Phi_m^0 \rangle = e^{im\theta}. \quad (2.36)$$

In the shells $j > 0$, the differential equation to solve is rather

$$\left[\frac{d^2}{dr^2} + \frac{1}{r} \frac{d}{dr} + \frac{1}{r^2} \frac{d^2}{d\theta^2} + k^2 n^2(r, \theta) \right] \psi = 0. \quad (2.37)$$

Inside each shell, we suppose that the potential strength depends only on the angular variable, i.e. $k^2 r^2 n^2(r, \theta) \mapsto k^2 r_j^2 n^2(r_j, \theta)$ such that the angular sampling of the refractive index is done at

$r = r_j$ for each shell. (2.37) is then amenable to a separation of variables

$$\left[\rho_j^2 \frac{d^2}{d\rho_j^2} + \rho_j \frac{d}{d\rho_j} - \xi^j \right] \mathcal{R}^j = 0 \quad (2.38a)$$

$$\left[\frac{d}{d\theta^2} + (k^2 n^2(r_j, \theta) r_j^2 + \xi^j) \right] \Phi^j = 0 \quad (2.38b)$$

where $\rho_j = r/r_j$ is the scaled radial variable of the shell. These equations can readily be solved by noticing that $\Phi^j(\theta + 2\pi) = \Phi^j(\theta)$. We expand the solution in a Fourier series

$$\langle \theta | \Phi_\mu^j \rangle = \frac{1}{\sqrt{2\pi}} \sum_{m=-\infty}^{\infty} c_{m\mu}^j e^{im\theta} \quad (2.39)$$

Projecting onto $|\Phi_m^0\rangle$ yields

$$\sum_{m=-\infty}^{\infty} \left[-m^2 \langle \Phi_{m'}^0 | \Phi_m^j \rangle + \xi^j \langle \Phi_{m'}^0 | \Phi_m^j \rangle + k^2 r_j^2 \langle \Phi_{m'}^0 | n^2(r_j, \theta) | \Phi_m^j \rangle \right] = 0 \quad (2.40)$$

Noticing that

$$\langle \Phi_{m'}^0 | \Phi_m^j \rangle = \sum_{\mu=-\infty}^{\infty} c_{m\mu}^j \delta_{mm'} \quad (2.41)$$

we can write

$$\sum_m \left[-m^2 \delta_{mm'} + \xi^j \delta_{mm'} + \frac{k^2 r_j^2}{2\pi} \int_0^{2\pi} n^2(r, \theta) e^{i(m-m')\theta} d\theta \right] c_{m\mu}^j = 0. \quad (2.42)$$

Using this last equation, we can set up an eigenvalue problem for the separation constant and the Fourier coefficients

$$\mathbf{L}^j \mathbf{c}_\mu^j = \xi_\mu^j \mathbf{c}_\mu^j \quad (2.43)$$

with

$$L_{mm'}^j = m^2 \delta_{mm'} - \frac{k^2 r_j^2}{2\pi} \int_0^{2\pi} n^2(r_j, \theta) e^{i(m-m')\theta} d\theta. \quad (2.44)$$

In the TE case, we must take $n \mapsto n_{\text{eff}}$. This leads us to evaluate the extra integral

$$I = \frac{1}{2\pi} \int_0^{2\pi} \left[\frac{1}{n} \frac{d^2 n(r_j, \theta)}{d\theta^2} - \frac{2}{n^2} \left(\frac{dn(r_j, \theta)}{d\theta} \right)^2 \right] e^{i(m-m')\theta} d\theta. \quad (2.45)$$

The numerical cost of this integral can be lessened if we notice that if we write it as a function of n^2 we obtain

$$I = \frac{1}{2\pi} \int_0^{2\pi} \left[\frac{1}{2n^2} \frac{d^2 n^2(r_j, \theta)}{d\theta^2} - \frac{3}{4n^4} \left(\frac{dn^2(r_j, \theta)}{d\theta} \right)^2 \right] e^{i(m-m')\theta} d\theta \quad (2.46)$$

which, in turn, can be rewritten as

$$I = \frac{1}{2\pi} \int_0^{2\pi} \left[\frac{1}{2} \frac{d^2 \log n^2(r_j, \theta)}{d\theta^2} - \left(\frac{1}{2} \frac{d \log n^2(r_j, \theta)}{d\theta} \right)^2 \right] e^{i(m-m')\theta} d\theta. \quad (2.47)$$

Integrating by parts twice yields

$$I = \frac{1}{2\pi} \int_0^{2\pi} \left[-\frac{(m-m')^2}{2} \log n^2(r_j, \theta) - \left(\frac{1}{2} \frac{d \log n^2(r_j, \theta)}{d\theta} \right)^2 \right] e^{i(m-m')\theta} d\theta. \quad (2.48)$$

The second term cannot be integrated out, but this final result means that we will only need to numerically evaluate the first derivative of the refractive index (although its analytical form could be provided).

Notice the form of the \mathbf{L}^j matrix. As can be seen from inspection, the value of the elements depend only on their distance from the diagonal. Taking a closer look reveals the form

$$\mathbf{L}^j = \mathbf{M}^2 + \begin{pmatrix} n_0 & n_{-1} & \cdots & \cdots & n_{-2M} \\ n_1 & n_0 & \cdots & \cdots & n_{-2M-1} \\ n_2 & n_1 & n_0 & \cdots & n_{-2M-2} \\ \vdots & n_2 & n_1 & \ddots & \vdots \\ n_{2M} & \cdots & \cdots & \cdots & n_0 \end{pmatrix} \quad (2.49)$$

which is manifestly Toeplitz. When the potential is real, the Fourier series has the property $n_{-j} = n_j^*$, which makes the \mathbf{L}^j matrix Hermitian. In the general case, however, it is not. Because we will need to use orthogonality relations in what follows, we must compute both the left and right eigenvectors. We will note the left (covariant) basis by $|\tilde{\Phi}_\mu^j\rangle$. This is not sufficient, however, because we are not guaranteed that both sets of eigenvectors will form a complete basis.

Now that we know the set of eigenvalues $\{\xi_\mu^j\}$, we can solve the radial equation (2.38a). It is instantly recognized as a Cauchy-Euler equation. Given its coefficients, one can write the solution as [21, p. 118-119]

$$\mathcal{R}_\mu^j(r) = a_\mu^j \rho_j^{+\sqrt{\xi_\mu^j}} + b_\mu^j \rho_j^{-\sqrt{\xi_\mu^j}}. \quad (2.50)$$

The solution is now known in all space. We can now apply the boundary conditions (2.12) at the interface of each shell $j \rightarrow j+1$. The process generates two sets of equations

$$\sum_\mu \left[a_\mu^j \rho_j^{+\sqrt{\xi_\mu^j}} + b_\mu^j \rho_j^{-\sqrt{\xi_\mu^j}} \right] |\Phi_\mu^j\rangle = \sum_\mu \left[b_\mu^{j+1} \rho_{j+1}^{+\sqrt{\xi_\mu^{j+1}}} + a_\mu^{j+1} \rho_{j+1}^{-\sqrt{\xi_\mu^{j+1}}} \right] |\Phi_\mu^{j+1}\rangle \quad (2.51a)$$

$$\eta_j \frac{d}{dr} \sum_\mu \left[a_\mu^j \rho_j^{+\sqrt{\xi_\mu^j}} + b_\mu^j \rho_j^{-\sqrt{\xi_\mu^j}} \right] |\Phi_\mu^j\rangle = \eta_{j+1} \frac{d}{dr} \sum_\mu \left[b_\mu^{j+1} \rho_{j+1}^{+\sqrt{\xi_\mu^{j+1}}} + b_\mu^{j+1} \rho_{j+1}^{-\sqrt{\xi_\mu^{j+1}}} \right] |\Phi_\mu^{j+1}\rangle \quad (2.51b)$$

where $\eta_j = 1/(n(r_j, \theta))$ in TM (TE) polarization. The interior scattering matrices are constructed via premultiplying by the left eigenvectors $|\tilde{\Phi}_\mu^j\rangle$ on each side. Combining both resulting equations leads to the linear system

$$\begin{pmatrix} \mathbf{A} & \mathbf{B} \\ \mathbf{C} & \mathbf{D} \end{pmatrix} \begin{pmatrix} \mathbf{a}^j \\ \mathbf{a}^{j+1} \end{pmatrix} = \begin{pmatrix} \mathbf{E} & \mathbf{F} \\ \mathbf{G} & \mathbf{H} \end{pmatrix} \begin{pmatrix} \mathbf{b}^j \\ \mathbf{b}^{j+1} \end{pmatrix} \quad (2.52)$$

which can be inverted using Schur's complements to yield a relationship between the \mathbf{a} and \mathbf{b} coefficients. The matrix relating the four sets of coefficients is an *interior scattering matrix*, \mathbf{S}^j . Physically, this relates the locally incoming waves from shell $j + 1$ in shell j to the locally outgoing from shell j to shell $j + 1$. The last necessary breakthrough is to realize that we can connect the solutions from shell j to those of the shell $j + 2$, then $j + 3$ and so on. When started from $j = 0$, this iterative process yields the relationship

$$\begin{pmatrix} \mathbf{a}^0 \\ \mathbf{B} \end{pmatrix} = \mathbf{S}^{0,N} \begin{pmatrix} \mathbf{a}^0 \\ \mathbf{A} \end{pmatrix} \quad (2.53)$$

such that the \mathbf{S} -matrix of the system is the block $\mathbf{S}_{22}^{0,N}$. More details can be found in Appendix C.1.

2.3.2 Numerical Analysis and Calibration

While numerical analysis has been heavily formalized in recent years, it is still as much an art as a science. In implementing the algorithm, we thus came across two potential problems: the inversion of the \mathbf{K} matrix (defined below) and the final Hadamard product $\mathcal{H} \circ \mathbf{S}_{22}^{0,N}$. We analyze the two issues and provide solutions to the instability they cause. We also calibrate the method with systems whose analytical solution is known: the homogeneous circular cavity and the annular cavity. We also compare our method to results obtained in the literature.

Numerical Back and Forth

At each step of the algorithm, we must invert a matrix of the form

$$\mathbf{K}^{j,j+1} = \left(\frac{r_j - \epsilon}{r_j + \epsilon} \right)^{\Lambda_j} - \tilde{\mathbf{S}}_{11}^{j+1} \left(\frac{r_j + \epsilon}{r_j - \epsilon} \right)^{\Lambda_j} \tilde{\mathbf{S}}_{22}^{0,j}. \quad (2.54)$$

Given that the elements of this matrix highly depend upon the discretization parameter ϵ , the half-width of the shells, we can use the condition number W of this matrix as an indicator of the quality of the discretization. It can be grossly estimated by the ratio of the maximum and minimum elements of the matrix. By assuming that there is no amplification in the system, all interior scattering matrices have $\|\mathbf{S}\| < 1$ and we can approximate

$$W \sim 1 + \frac{4\lambda_{\max}\epsilon}{r_j}. \quad (2.55)$$

The λ_{\max} parameter depends solely on the Fourier components of the refractive index. Given that most cavities that will study will be mildly inhomogenous, i.e. that $|n_0| \geq |n_m|$, we posit the upper bound $|\lambda_{\max}| < 3nkR_0$. A good choice of ϵ is thus

$$\epsilon \ll \frac{1}{12nk} \ll \frac{\lambda}{2n} \quad (2.56)$$

which mirrors the conventional wisdom. This empirical rule is applied in every computation in this thesis.

Introduction to Gerschgorin circles and possibility of inversion problems of \mathbf{K} .

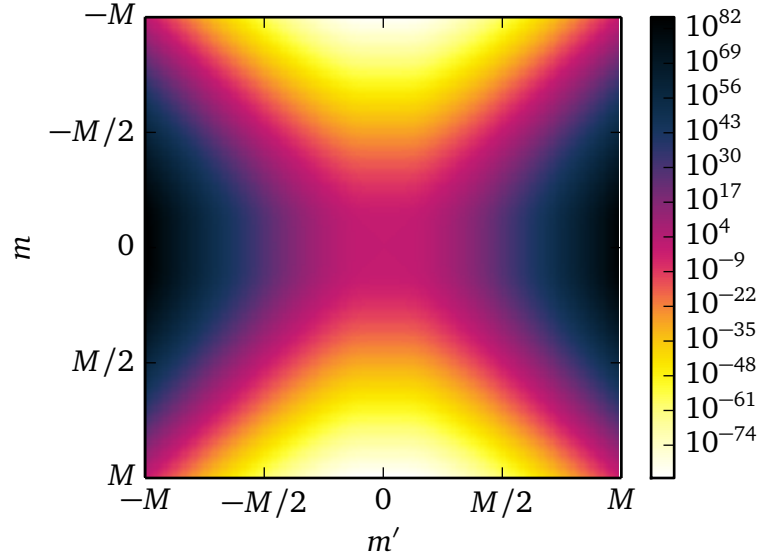


Figure 2.4 – General form of absolute value of the Hankel matrix \mathcal{H} . We have used the parameters $z = 10$ and $M = 100$, but the pattern scales with M and z .

Hadamard Product

Like Frodo before Mount Doom, we must face a final challenge before conquering upon all evil, or, in our case, computing the scattering matrix. Our final demon takes the form of the product

$$\mathbf{S} = [\mathbf{H}^{(+)}]^{-1} \mathbf{S}_{22}^{0,N} \mathbf{H}^{(-)} \quad (2.57)$$

where the \mathbf{H} are diagonal matrices with entries $H_m^{(\pm)}(n_o k R_0)$. We recast the matrix product as a Hadamard (element-wise) product

$$\mathbf{S} = \mathcal{H} \circ \mathbf{S}_{22}^{0,N} \quad (2.58)$$

with $\mathcal{H}_{mm'} = H_m^{(-)}(n_o k R_0) / H_{m'}^{(+)}(n_o k R_0)$. A quick peek at Fig. 2.4 announces the disaster. The region $|m'| > |m|$ increases exponentially with $|m'| - |m|$. This wouldn't be an issue if the corresponding elements of the block scattering matrix $\mathbf{S}_{22}^{0,N}$ were exponentially decreasing (as we physically expect them to); however, the numerical construction of this matrix implies the addition and subtraction of $\mathcal{O}(1)$ floating-point numbers, limiting their range to about 10^{-15} , the decimal accuracy associated with double precision arithmetic. Consequently, the final Hadamard product yields scattering matrices with unphysically large off-diagonal elements.

Several solutions have been considered, e.g. the use of matrix masks and of higher precision arithmetic. The latter was swiftly abandoned due to the difficulty of the implementation[†], even though it could help stabilize the numerical algorithm [22, §5.8.4]. The use of matrix masks is

[†]Even if we disregard the fact that no C++ compiler support the IEEE 754 binary128 quadruple precision float-point representation, we would still need to find numerical libraries that extend the BLAS and LAPACK libraries to work at higher precision.

made possible by noting that the cavity cannot convert arbitrarily high angular momenta. The maximum angular momentum it can affect, M_{\max} is a function of its “degree of inhomogeneity”, characterized by the absolute size of the Fourier components of the refractive index (which also depend on the geometry of the cavity). This gives the \mathbf{S} -matrix a banded form. The width of this band could be detected in $\mathbf{S}_{22}^{0,N}$ before taking the Hadamard product. After the product, all elements outside this band could be set to zero. The interested reader might want to go through Türeci’s discussion of the banded form and the numerical problems associated with the Hankel matrices [23, §3.4].

Show the
S-matrix
of the
quadrupo-
lar cavity

We have, however, chosen a different path. It turns out that relation (2.31) precisely relates the diverging parts of the Hankel matrix to its vanishing one. Imposing this symmetry on the numerical scattering matrix allows the algorithm to return physical scattering matrices.

Calibration

One of the most important step in algorithmic creation is the *calibration phase*. Ours was calibrated against two cavities: the homogeneous circular cavity and the annular cavity. Their analytical form is given below.

The scattering matrix of the homogeneous circular cavity is trivially obtained. Assuming that the refractive index inside the cavity is n_c and n_o outside, the solution inside the cavity is given by

$$\psi^c = \sum_m a_m^c J_m(n_o k r) e^{im\theta} \quad (2.59)$$

while the solution outside the cavity is given by (2.15). Imposing the electromagnetic boundary conditions yields two infinite sets of equations for three sets of coefficients. Solving yields a linear relationship between the A_m and B_m sets, viz. the scattering matrix

$$S_{mm'}^{\text{HD}} = -\frac{\eta_{co} J'_m(Z_c) H_m^{(-)}(Z_o) - J_m(Z_c) H_m^{(-)'}(Z_o)}{\eta_{co} J'_m(Z_c) H_m^{(+)}(Z_o) - J_m(Z_c) H_m^{(+)'}(Z_o)} \delta_{mm'}. \quad (2.60)$$

where $Z_c = n_c k R_0$, $Z_o = n_o k R_0$ and $\eta_{co} = n_c/n_o$ (n_o/n_c) in TM (TE) polarization.

Calibration with homogeneous circular cavity. Identification of zeroes with peaks of delay matrix. Computation of the zeros in the complex plane.

Derivation of the scattering matrix of the annular cavity is a little more involved. Suffice it to say that it is given by

$$\mathbf{S}^{\text{AC}} = -\left[n_o \mathbf{H}^{(-)'}(Z_o) - n_c \mathbf{H}^{(-)}(Z_o) \mathbf{G} \mathbf{F}^{-1} \right] \left[n_o \mathbf{H}^{(+)'}(Z_o) - n_c \mathbf{H}^{(+)}(Z_o) \mathbf{G} \mathbf{F}^{-1} \right]^{-1} \quad (2.61)$$

where

$$\mathbf{F} = \mathbf{H}^{(-)}(Z_c) + \mathbf{H}^{(+)}(Z_c) \mathbf{S}^{\text{HD}} \quad \mathbf{G} = \mathbf{H}^{(-)'}(Z_c) + \mathbf{H}^{(+)'}(Z_c) \mathbf{S}^{\text{HD}}. \quad (2.62)$$

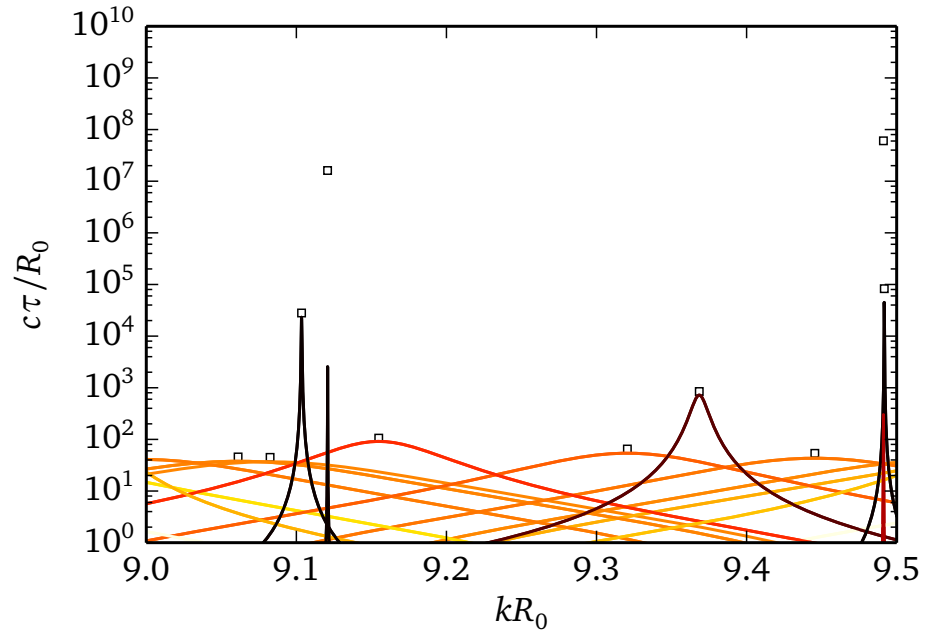


Figure 2.5 – Time delay spectrum of a circular cavity with $n_c = 3.2$ and $n_o = 1$. The squares represent the complex position of the poles of the scattering matrix. The equivalent time delay is computed using $c\tau/R_0 = -\text{Re}(kR_0)/2\text{Im}(kR_0)$.

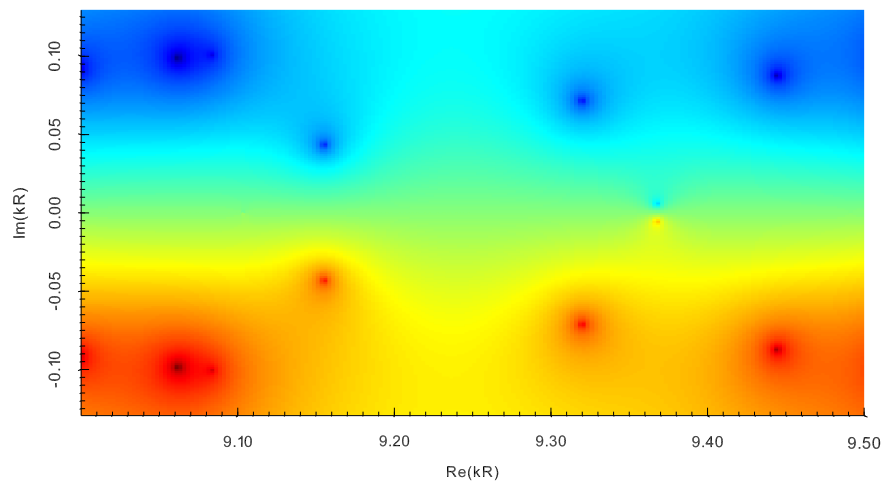


Figure 2.6 – Mirror symmetry of the scattering matrix.

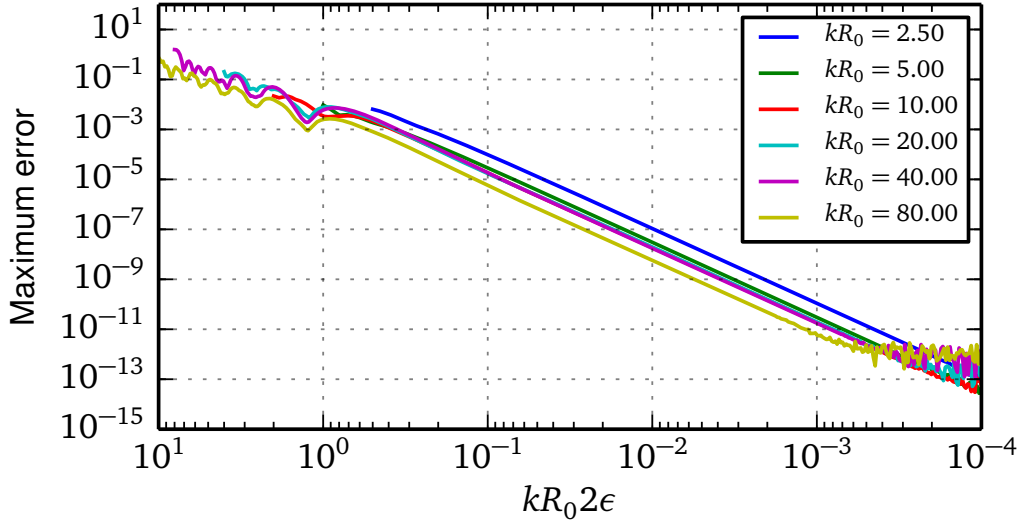


Figure 2.7 – Calibration of SQA against the homogeneous disk. The cavity has refractive index $n_c = 1.5$ and is embedded in air $n_o = 1$. The exterior radius is set to $R_0 = 1$ and we take the number of shells to be $N = 2$. The error approximately follows a cubic power-law behaviour in the discretization size.

A proper derivation can be found in [24]; an improved one can be found in [9, Appendix D].

Calibration with annular cavity.

Comparison with results in the literature.

2.4 Case Study: Gaussian Deformation of the Refractive Index

As an academic demonstration of the power of the method, we present a study of a circular cavity whose refractive index has a Gaussian shape

$$n(r, \theta) = n_0 + \delta n \exp \left[-\frac{r^2 + 2dr \cos(\Theta - \theta) + d^2}{2w^2} \right], \quad (2.63)$$

where n_0 is the background refractive index, δn the deformation amplitude, w its half-width and (d, Θ) its position relative to the center of the cavity.

As previously noted by G. P-A. [9], a peculiar duality exists between high-Q resonances and directional emission. Working with a cavity similar to the annular one, it stands to reason that we will recover the same pattern. However, this study will be used as a stepping stone for our inquiries in the realm of non-uniformly pumped active microcavities.

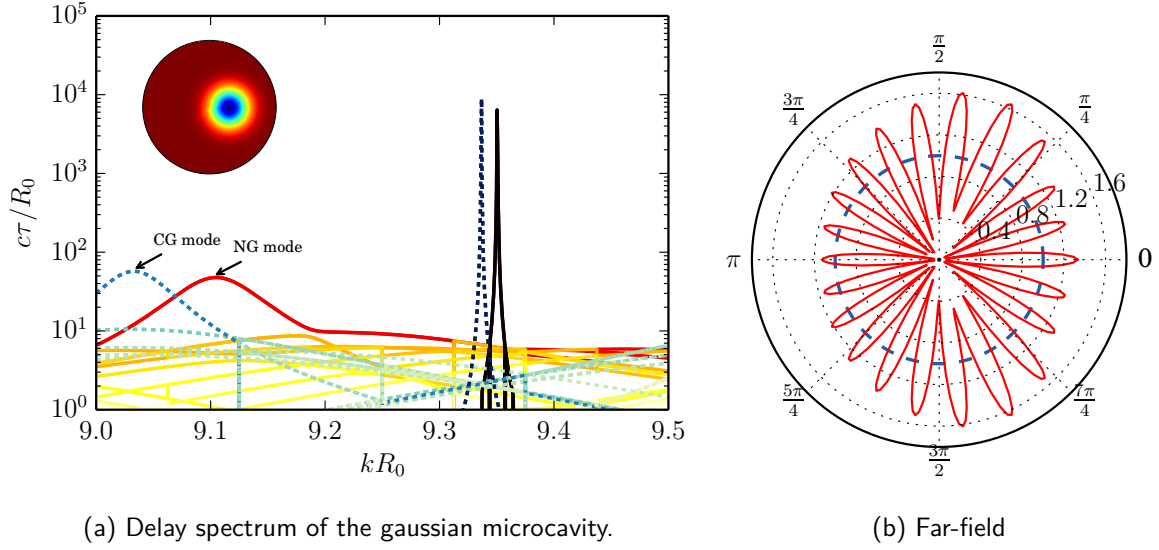


Figure 2.8 – Delay spectrum and far-field.

2.4.1 Loss of Integrability and the KAM Scenario

When $d = 0$, the potential is central and angular momentum is necessarily conserved. If the system is also unitary (no absorption nor gain), it can be shown that the system is integrable[‡]. This conservation of angular momentum in turn implies circular symmetry of the fields and hence of the far-field radiation pattern. Since most applications (particularly lasers) require a certain directionality in the emission, our goal is to break the circular symmetry in such a way as to minimize the degradation of the finesse (Q -factor) and maximizing the output directionality. Historically, this goal has spawned the research field of ARCs wherein the boundary of the circular cavity is parametrically deformed to yield limaçon, stadium, elliptical, quadrupolar, etc. shapes.

2.4.2 Numerical Results

2.4.3 Geodesics and Ray Analysis

While our numerical method allows us to perform full-wave simulations of cavities, it is often useful to consider the associated billiard system, which is the small wavelength approximation of Helmholtz's equation. In homogeneous ARCS, photons follow straight path trajectories and are specularly reflected at the interfaces. In inhomogeneous ARCs, photons follow curved trajectories that obey Fermat's principle. The general equations defining those *geodesic* paths can be found by using the metric

$$(dt)^2 = g_{\mu\nu} dx^\mu dx^\nu. \quad (2.64)$$

[‡]The covariant form of Maxwell's equation and their associated Euler-Lagrange equation make this conservation perfectly clear.

The time it takes to travel a particular trajectory is given by

$$t = \int_{\lambda_0}^{\lambda_1} \sqrt{g_{\mu\nu} \dot{x}^\mu \dot{x}^\nu} d\lambda \quad (2.65)$$

where λ is a parameter of the curve. Applying the Euler-Lagrange equation

$$\frac{\partial L}{\partial x^\alpha} - \frac{d}{d\lambda} \frac{\partial L}{\partial \dot{x}^\alpha} = 0 \quad (2.66)$$

on the functional $L = \sqrt{w} = \sqrt{g_{\mu\nu} \dot{x}^\mu \dot{x}^\nu} d\lambda$ minimizes the time it takes to travel from one point to another. Evaluating the derivatives

$$\begin{aligned} 0 &= \frac{\partial(\sqrt{w})}{\partial x^\alpha} - \frac{d}{d\lambda} \frac{\partial(\sqrt{w})}{\partial \dot{x}^\alpha} \\ &= \frac{\partial w}{\partial x^\alpha} + \frac{1}{2\sqrt{w}} \frac{dw}{d\lambda} \frac{\partial w}{\partial \dot{x}^\alpha} - \frac{d}{d\lambda} \frac{\partial w}{\partial \dot{x}^\alpha} \end{aligned}$$

When λ is an affine parameter, the derivative $dw/d\lambda$ vanishes [25, 26] and the Euler-Lagrange equation becomes

$$\begin{aligned} \frac{\partial w}{\partial x^\alpha} &= \frac{d}{d\lambda} \frac{\partial w}{\partial \dot{x}^\alpha} \\ g_{\mu\nu, \alpha} \dot{x}^\mu \dot{x}^\nu &= \frac{d}{d\lambda} [g_{\mu\nu} \delta_\alpha^\mu \dot{x}^\nu + g_{\mu\nu} \delta_\alpha^\nu \dot{x}^\mu] \\ &= \frac{d}{d\lambda} [g_{\alpha\nu} \dot{x}^\nu + g_{\mu\alpha} \dot{x}^\mu] \\ &= g_{\alpha\nu, \lambda} \dot{x}^\lambda \dot{x}^\nu + g_{\alpha\nu} \ddot{x}^\nu + g_{\mu\alpha, \lambda} \dot{x}^\lambda \dot{x}^\mu + g_{\mu\alpha} \ddot{x}^\mu \quad (\text{chain rule: } \frac{dg_{\mu\nu}}{d\lambda} = \frac{\partial g_{\mu\nu}}{\partial x^\lambda} \frac{dx^\lambda}{d\lambda}) \\ g_{\alpha\nu, \lambda} \dot{x}^\lambda \dot{x}^\nu + g_{\mu\alpha, \lambda} \dot{x}^\lambda \dot{x}^\mu &= \dot{x}^\mu \dot{x}^\nu [g_{\mu\nu, \alpha} - g_{\alpha\nu, \mu} - g_{\alpha\mu, \nu}] \quad (\text{collecting differentiation orders}) \\ \delta^\sigma_\mu \ddot{x}^\mu &= \frac{1}{2} g^{\sigma\alpha} [g_{\mu\nu, \alpha} - g_{\alpha\nu, \mu} - g_{\alpha\mu, \nu}] \dot{x}^\mu \dot{x}^\nu \quad (\text{symmetry of } g_{\mu\nu} \text{ and } \times g^{\sigma\alpha}) \end{aligned}$$

This finally yields the equation

$$\ddot{x}^\sigma + \Gamma^\sigma_{\mu\nu} \dot{x}^\mu \dot{x}^\nu = 0 \quad (2.67)$$

where $\Gamma^\sigma_{\mu\nu}$ are the Christoffel symbols of the second kind.

Discuss the results.

Discuss the geodesics in this geometry.

2.5 Perspectives

Optimization of refractive index profile and geometry for specific purposes.

Optimization of pump profile, refractive index profile and geometry for specific purposes.

Use of integral methods to numerically solve scattering problem (may lead to more stable algorithms).

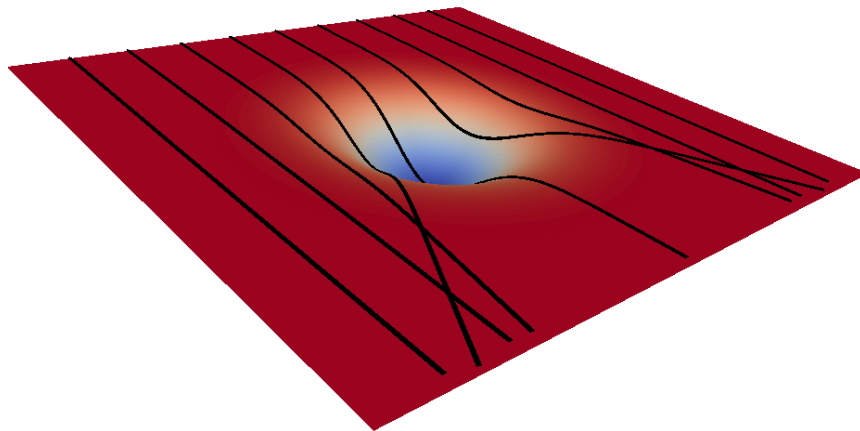


Figure 2.9 – Trajectories for photons of different impact parameters. The trajectories are the geodesics of the relevant “optical spacetime”, where the curvature of space represents the optical distance that the photon has to traverse. The central region, where the refractive index is lower, acts as a diverging lens.

Chapter 3

Active Media and Radiation

While the previous chapter dealt with the modelization of passive dielectric structures, this one will attempt to model more complex classes of structures.

The first part will deal with active dielectric cavities. A recently formulated steady state *ab initio* laser theory (SALT) solves the Schrödinger-Bloch state equations in such a way that the effect of the active medium can be considered as a pump-dependent deformation of the refractive index profile.

The second part attempts to model

3.1 Lasing and Scattering

3.1.1 Modeling the Quantum Gain Medium

Primer on SALT and its derivation for TM/TE modes.

3.1.2 Variable Phase Method

Primer on VPM for bidimensional cavities (mention its use for 3D cavities with vector spherical wave functions).

Motivation for VPM: computing the field more efficiently than in SQA.

3.1.3 Scattering in 3D and Antennae

Somewhat departing from the previous chapter, we here present three different methods to compute the current distribution on an arbitrary antenna. First, we will state the usual result from

[27] and then we will take the scattering viewpoint.

From our previous viewpoint that sources generate electric and magnetic fields and using Maxwell's equations outside the region where the sources are, we can obtain [27]

$$\iiint_V \mathbf{K}(\mathbf{r}, \mathbf{r}') J(\mathbf{r}') d\mathbf{r}' = i\omega \mathbf{E}(\mathbf{r}) \quad (3.1)$$

where the kernel $\mathbf{K}(\mathbf{r}, \mathbf{r}')$ is

$$\mathbf{K}(\mathbf{r}, \mathbf{r}') = (\nabla^2 + k^2) \frac{e^{ik|\mathbf{r}-\mathbf{r}'|}}{4\pi|\mathbf{r}-\mathbf{r}'|} \quad (3.2)$$

For antennae made of perfect conductors ($\sigma \rightarrow \infty$), we must have $\mathbf{E} \rightarrow 0$ except in the feeding region. If \mathbf{E} is known in the feeding region, this becomes an integral equation for the unknown current distribution. Specifically, it becomes a vectorial Fredholm equation of the first kind. Its vectorial nature makes it more difficult to solve.

It is unknown to the author of this report why Elliott insists on separating the electric field and the current. By using Ohm's law, we can arrive at integral equations which have a single unknown. This is the scattering viewpoint.

Consider an antenna of arbitrary geometry and arbitrary permittivity and conductivity but of vacuum permeability embedded in an infinite medium of constant permittivity $\epsilon_B(\omega)$. For non-magnetic materials and harmonic time-dependence, the curl equation for the electric field is

$$\begin{aligned} \nabla \times \nabla \times \mathbf{E} &= ik[\nabla \times \mathbf{H}] \\ &= ik[-ik\epsilon_B(\omega)\mathbf{E} + \mathbf{J}] \\ &= k^2 \left[\epsilon_B(\omega)\mathbf{E} - \frac{\sigma}{ik}\mathbf{E} \right] \\ &= k^2\epsilon_B(\omega)\mathbf{E} \end{aligned}$$

where we used Ohm's law

$$\mathbf{J} = \sigma \mathbf{E} \quad (3.3)$$

and redefined

$$\epsilon_B(\omega) \mapsto \epsilon_B(\omega) + i\sigma/k \quad (3.4)$$

For our antenna, the curl equation for the electric field become

$$\nabla \times \nabla \times \mathbf{E} = k^2\epsilon_B(\omega)\mathbf{E} \quad \mathbf{r} \notin V_{\text{scat}} \quad (3.5a)$$

$$\nabla \times \nabla \times \mathbf{E} = k^2\epsilon(\mathbf{r}; \omega)\mathbf{E} \quad \mathbf{r} \in V_{\text{scat}} \quad (3.5b)$$

By subtracting $k^2\epsilon_B(\omega)\mathbf{E}$ from both sides of the second equation, we obtain an equation that is valid both inside and outside the antenna (or scatterer)

$$\nabla \times \nabla \times \mathbf{E} - k^2\epsilon_B(\omega)\mathbf{E} = k^2\Delta\epsilon(\mathbf{r}; \omega)\mathbf{E} \quad \forall \mathbf{r} \quad (3.6)$$

where

$$\Delta\epsilon(\mathbf{r}; \omega) = \epsilon(\mathbf{r}, \omega) - \epsilon_B(\omega). \quad (3.7)$$

The vector equation (3.6) has a formal solution in terms of a dyadic Green's function [28] and an incident field [29]

$$\mathbf{E}(\mathbf{r}) = \mathbf{E}_{\text{inc}}(\mathbf{r}) + k^2 \iiint_{V_{\text{scat}}} \mathbf{G}(\mathbf{r}, \mathbf{r}') \Delta\epsilon(\mathbf{r}') \mathbf{E}(\mathbf{r}') d\mathbf{r}' \quad (3.8)$$

where the Green's function is given by, in coordinate-free representation

$$\mathbf{G}(\mathbf{r}, \mathbf{r}') = \left(\mathbf{I} + \frac{1}{k\sqrt{\epsilon_B}} \nabla \nabla \right) g(\mathbf{r}, \mathbf{r}') \quad (3.9)$$

$$g(\mathbf{r}, \mathbf{r}') = \frac{\exp(i\sqrt{\epsilon_B}k|\mathbf{r} - \mathbf{r}'|)}{4\pi|\mathbf{r} - \mathbf{r}'|}. \quad (3.10)$$

We note that this is a multidimensional, vector Fredholm integral equation of the second kind with singular kernel $\mathbf{G}(\mathbf{r}, \mathbf{r}') \Delta\epsilon(\mathbf{r}')$.

Let's take a moment to take in equation (3.8). It is the general solution to the scattering of light on *any* non-magnetic material. The material can be inhomogeneous, anisotropic, of arbitrary geometry and even non-linear. Moreover, it considers the complete vector field: we are not forced to set TM/TE polarization. This generality, however, comes at a cost. While uni-dimensional Fredholm equation of the second type are usually easily solvable (even when the kernel is singular) [30], the multidimensional case is intractable unless we use basis function expansion to factor out the angular dependence of the field and kernel. This is what is done in [29] in the case of linear, isotropic, spherical scatterers.

The situation is further complicated by the fact that the kernel of the integral equation is singular. One way to remedy this problem is to embrace the singularity. Given the form of the Green dyadic, a way to construct an integration routine would be to notice that, if r and r' are the amplitudes of the vectors

$$\frac{1}{|\mathbf{r} - \mathbf{r}'|} = \frac{1}{r_{>}} \sum_{\ell=0}^{\infty} \left(\frac{r_{<}}{r_{>}} \right)^{\ell} P_{\ell}(\cos \gamma) \quad (3.11)$$

where γ is the angle between \mathbf{r} and \mathbf{r}' , $r_{<} = \min(r, r')$, $r_{>} = \max(r, r')$. This allows us to factor out the singular part of the kernel. There will then be poles of orders up to $\ell + 1$ which we can use as a weight for an integration routine.

Experience tells us that multidimensional integration is never easy and computationally costly. We will steer away from this method of solution from the time being. Of course, by expanding the solution in vector spherical harmonics, we could factor the radial singularity and construct an appropriate single dimensional integration routine. This will be the basis of our next, and adopted, solution.

3.1.4 Effective Index Approximation

In our last report, we derived general equations for the behaviour of light in bidimensional structures, approximating the finite thickness resonator by an infinite thickness one. In what follows, we will rigorously take into account the finite thickness of the bidimensional resonator. Having these exact equations might enable us to study the bidimensional limit of the electromagnetic theory.

Given the coordinate-free representation of the Green dyadic, we can solve the scattering problem in cylindrical coordinates. Say we have a thin dielectric resonator of thickness t_z whose boundary is given by the function $R(\phi)$. The refractive index inside the dielectric is given by $\epsilon = \epsilon(r, \phi)$ and is constant outside. We have (if the functional dependence is omitted, it is implicitly assumed to be on \mathbf{r})

$$\mathbf{E} = \mathbf{E}_{\text{inc}} + k^2 \int_0^{R(\phi)} \int_0^{2\pi} \int_{-t_z/2}^{t_z/2} \mathbf{G}(\mathbf{r}, \phi, z | \mathbf{r}', \phi', z') \Delta\epsilon(r', \phi') \mathbf{E}(r', \phi', z') dz' d\phi' dr' \quad (3.12)$$

Perhaps the simplest way to retain the simplicity of the integrals is to expand the fields and the dyadic Green's function in vector cylindrical harmonics. However, this expansion requires the evaluation of an integral [31], making for intensive numerical work.

One other way to approach this would be to evaluate the integrals in spherical coordinates. In that case, we could separate the angular behaviour from the radial behaviour and end up with a uni-dimensional Fredholm equation which we could solve by using either the resolvent formalism or linear algebra techniques. Using spherical coordinates does not exploit the symmetry of the problem and leads to complicated integration limits, however.

3.2 Basic Antenna Theory and HFSS Simulations

Even today, a full 140 years after the publication of Maxwell's *Treatise on Electricity and Magnetism*, the electromagnetic modeling of radiating structures is an ongoing research problem. The notorious difficulty of solving Maxwell's equations seriously hampers analytical efforts and, due to the nature of electromagnetic radiation, numerical progress is not easier to achieve.

In what follows, we present the basic equations of antenna theory (Maxwell's) and discuss the nature of sources in this framework (currents and charges).

3.2.1 Maxwell's Equations

Being, by now, comfortable with the basic form of Maxwell's equations, we will simply state them for linear, non-chiral and reciprocal media and allow for the existence of current and charge

densities. They are (in Lorentz-Heaviside units with $c = 1$) [28]

$$\nabla \times \mathbf{E} + \frac{\partial(\mu\mathbf{H})}{\partial t} = 0 \quad (3.13a)$$

$$\nabla \times \mathbf{H} - \frac{\partial(\epsilon\mathbf{E})}{\partial t} - \mathbf{J}_c = \mathbf{J}_s \quad (3.13b)$$

$$\nabla \cdot (\epsilon\mathbf{E}) = \rho \quad (3.13c)$$

$$\nabla \cdot (\mu\mathbf{H}) = 0 \quad (3.13d)$$

where we have separated the current using two terms: a source current, \mathbf{J}_s and an induced conduction current \mathbf{J}_c . The induced conduction current is related to the electric field via Ohm's law, i.e.

$$\mathbf{J}_c = \sigma\mathbf{E} \quad (3.14)$$

while the source current is a prepared, physical source initially independent of the system.

A technical point is in order. In the antenna literature, the induced currents and charge density are considered as the fundamental quantities that *produce* the fields. While worthwhile (see the Stratton-Chu section), this viewpoint requires that either (i) we have *a priori* knowledge of the sources ($\mathbf{J}_t = \mathbf{J}_c + \mathbf{J}_s$ and ρ) or (ii) that we use the constitutive relations down the line. The first case applies to situations where the induced current is trivially known (e.g. the dipole antenna) or when $\sigma = 0$ and \mathbf{J}_s is known.

Also, even though the \mathbf{H} field was introduced as an auxiliary field to take into account the effect of an applied magnetic field to the material, we take it as the fundamental field as it leads to more easily solvable equations and is a completely equivalent choice.

3.2.2 Stratton-Chu Solution

In antenna problems, we want to compute the field values as a function of the sources that contribute to these fields. From electrostatics, we know that a current density \mathbf{J} gives rise to an electric field and a charge density ρ gives rise to a magnetic field. In the time-varying picture, the electric and magnetic fields become coupled and we take the viewpoint that the \mathbf{J} and ρ give rise to both electric and magnetic fields.

To compute the field from these sources, which are presupposed to exist, we must use the Stratton-Chu integrals. The derivation is standard, so we refer to [27]. Consider a volume V of free space containing sources and possibly excluded subvolumes V_i bound by surfaces S_i that contain matter of some kind. By the use of Green's and Stokes' theorems and other vectorial

identities, we find that the field outside the excluded subvolumes can be expressed as

$$\mathbf{E} = \frac{1}{4\pi} \iiint_V (\rho \nabla G + i\omega G \mathbf{J}) dV + \frac{1}{4\pi} \oint\oint_{S_1, \dots, S_N} [\mathbf{n} \cdot \mathbf{E} \nabla G + (\mathbf{n} \times \mathbf{E}) \times \nabla G + i\omega G (\mathbf{n} \times \mathbf{H})] dS \quad (3.15)$$

$$\mathbf{H} = \frac{1}{4\pi} \iiint_V \mathbf{J} \times \nabla G dV + \frac{1}{4\pi} \oint\oint_{S_1, \dots, S_N} [-i\omega G (\mathbf{n} \times \mathbf{E}) + (\mathbf{n} \times \mathbf{H}) \times \nabla G + (\mathbf{n} \cdot \mathbf{H}) \nabla G] dS \quad (3.16)$$

where G is the Green's function of the problem

$$G(\mathbf{r}, \mathbf{r}') = \frac{e^{ik|\mathbf{r}-\mathbf{r}'|}}{4\pi|\mathbf{r}-\mathbf{r}'|}. \quad (3.17)$$

These two equations are rigorous solutions of Maxwell's equations. They can be used with any antenna and provide ways to compute the current distribution if is unknown (constitutes an integral equation in the current) and can be used to compute the far-field of antennae when either (i) the current distribution is known or (ii) the near-field around the antenna is known. These two properties discriminate antennae into two categories, denoted Type I and Type II.

Type I antennae have a well-approximated current distribution, which means that there are no subvolumes to be excluded and therefore no surface integrals in expressions (3.15) and (3.16).

On the other hand, Type II antennae have well-approximated near-fields, leading us to exclude the volume containing the antenna. Expressions (3.15) and (3.16) contain only surface integrals, then.

3.2.3 Antenna Parameters

In the design of our antenna, we will want to optimize the value of some parameters. We will now describe some of these parameters.

Directivity and Gain [27, §1.16]

Given a radiation pattern measured (in the far-field) as the power density $\mathcal{P}(\theta, \varphi)$, we can define its *directivity* as

$$D(\theta, \varphi) = \frac{4\pi \mathcal{P}(\theta, \varphi)}{\int_0^\pi \int_0^{2\pi} \mathcal{P}(\theta', \varphi') \sin \theta' d\theta' d\varphi'}. \quad (3.18)$$

The value of the directivity is less than unity if the power density radiated at angle (θ, φ) is less than the average power radiated. For instance, an isotropic antenna will possess a unit directivity for all angles while a highly directional antenna will have a sharp peak in its directivity function at some angle (θ, φ) .

Another interesting concept to introduce is *partial directivity*. The power density can be divided into two contributions: the θ -polarized and the φ -polarized polarization and we can write

$$\mathcal{P}(\theta, \varphi) = \mathcal{P}_\theta(\theta, \varphi) + \mathcal{P}_\varphi(\theta, \varphi) \quad (3.19)$$

where the subscripts indicate the polarization state. The partial directivities hence follow

$$D(\theta, \varphi) = D_\theta(\theta, \varphi) + D_\varphi(\theta, \varphi). \quad (3.20)$$

We can also introduce the gain, which characterizes the loss and the directivity of the antenna simultaneously. It is simply given as

$$G(\theta, \varphi) = \frac{4\pi r^2 \mathcal{P}(\theta, \varphi)}{P} \quad (3.21)$$

where P is the power accepted by the antenna. Because of the losses, $P/r^2 > \int_0^\pi \int_0^{2\pi} \mathcal{P}(\theta', \varphi') \sin \theta' d\theta' d\varphi'$ such that $G(\theta, \varphi) < D(\theta, \varphi)$.

We can also define partial gains in the exact same fashion we defined partial directivities.

Radiation efficiency η is defined as the ratio of the total radiated power to the power accepted by the antenna [32].

Scattering Parameters

The scattering parameters (or S -parameters) are usually defined through a linear N -port network. Suppose we have an electronic device comprising N ports, or points of entry. Imagine shining light onto one of the ports, say port j . A certain percentage of the power carried by this light be reflected by this port and the rest will be transmitted to the other ports or absorbed in the medium. The *reflection* coefficient is given by S_{jj} while the transmission coefficients are given S_{ji} ($i \neq j$) where \mathbf{S} is the scattering matrix of the network. In a reciprocal (in the sense of Lorentz) network, the scattering matrix will be equal to its transpose, i.e. $S_{ij} = S_{ji}$. In a lossless network, the scattering matrix will be unitary.

This is, of course, highly reminiscent of the scattering operator in quantum-mechanical scattering which relates the outgoing (scattered) components to the incoming (incident) components

$$|\Psi_{\text{out}}\rangle = \mathcal{S} |\Psi_{\text{in}}\rangle. \quad (3.22)$$

In this case, the “ports” are the different angular momenta components rather than physical input/output connections. Ports are somewhat arbitrary in optical structures.

3.2.4 HFSS Simulations of an LCX Antenna

In our quest of finding a fibre-antenna design that can easily be integrated into textile, we have stumbled upon the leaky coaxial cable (LCX) design: a basic coaxial cable from which are cut

windows as to expose the dielectric core. The radiation characteristics can be tuned by changing the geometric properties of the windows.

LCX antennae are usually analyzed using harmonic analysis [33]. In our case, however, we cannot consider the structure to be periodic, as the total length of the fibre-antenna is of the order of the wavelength ($\lambda \sim 12\text{cm}$) and the period of the slots is smaller than the wavelength. Moreover, given the size of the slots, the author is comfortable to say that we neither are in the perturbation regime. Figure 3.3 shows the actual design and the important parameters.

Given the wild scale in the size of the structures (from the nanometer to the millimeter), we use the FEM to solve the driven problem. The parameters of interest will be the scattering parameters, the radiation pattern and antenna efficiency, gain and directivity. We will first model the fibre-antennae that were fabricated. There will be a subsequent optimization phase.

Preliminary Results

We first model the RF21 design. Its parameters are summarized in Table 3.1a.

Notice the small thickness of the silver layers (126 and 101 nm) compared to the other sizes involved. It takes a highly non-uniform mesh to model these small relative sizes. Moreover, since the silver has a high conductivity, it takes an even smaller mesh to model. Our first attempts at modeling this structure proved unsuccessful.

In the experimental data (see Figure 3.6), we see deep dips in the transmission spectrum (S_{12}) at approximately 1.8 GHz and 3 GHz. There are corresponding dips in the reflection parameters, S_{11} and S_{22} , which leads us to believe that remaining power was radiated through the slots. The existence of two dips seems predicated on the asymmetry of the fibre ($d_L \neq d_R$).

We also notice that the simulation data does not in any way correlate to the experimental data. This is probably due to the fact that, in our HFSS model, we had to put the thickness of the silver layers to $2\mu\text{m}$ instead of the values listed in Table 3.1a. In this regime, the fibre-antenna behaves like an ordinary transmission line. However, as the mesher does not allow us to go under $2\mu\text{m}$, we cannot conclude that is really due to the thickness of the Ag layers, only suspect it.

In our following report, we will break down the problem to make it analytically tractable and try to analyze the effect of “small” silver layers on the propagation of light.

3.3 Antenna Modelization

The goal of this project is to develop an antenna that is compatible with WiFi standards (i.e. emits at $f = 2.45\text{GHz}$) and easily integrated to textile. These two requirements impose multiple restrictions on both the materials that can be used and the geometry of the antenna. For seamless integration, we would like the antenna to be spun directly into the textile.

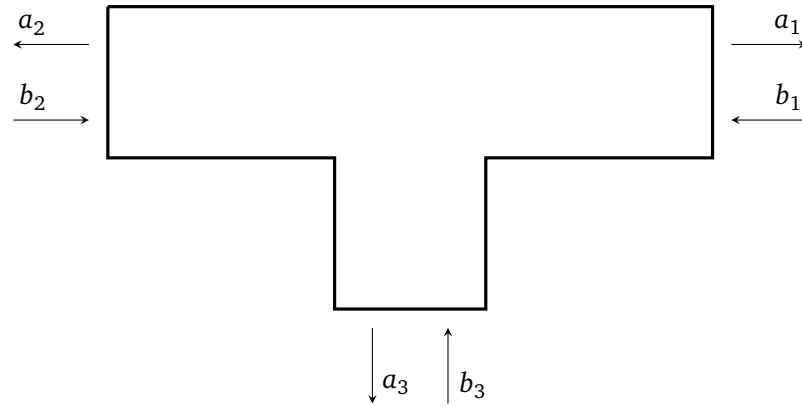


Figure 3.1 – Example of a 3-port network. The “ends” of the structure are generally used at its ports.

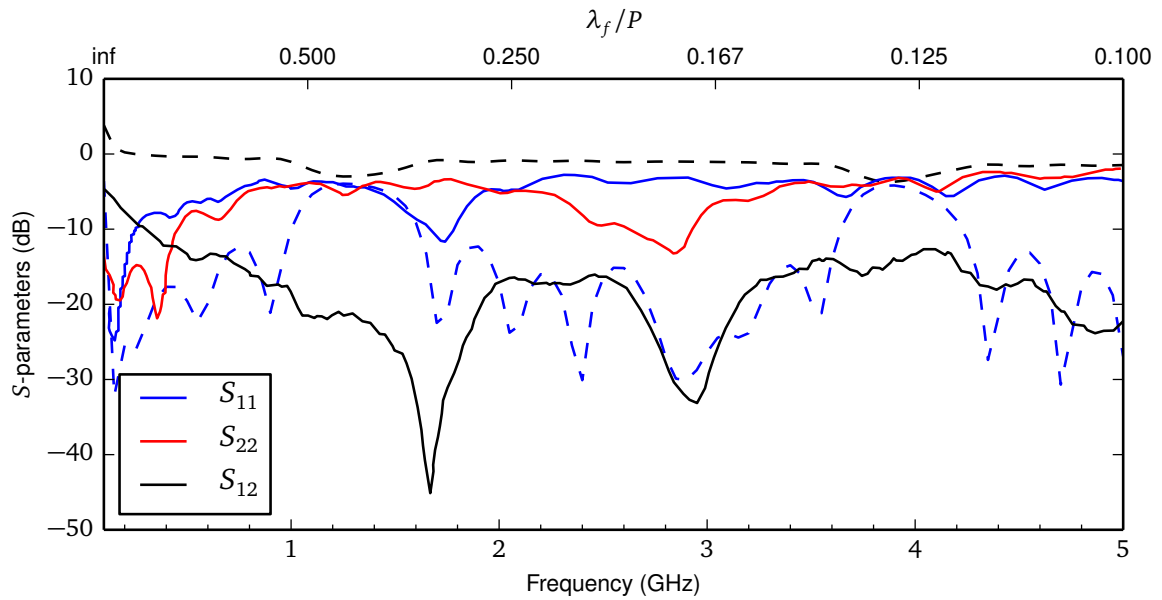


Figure 3.2 – S -parameters of the RF21 fibre design. The full lines represent the experimental data while the dotted lines represent the simulation data. The top x axis shows the S -parameters as a function of the ratio of the vacuum wavelength λ_f over the period of the windows P .

Most solutions today merely affix a patch antenna to a less encumbered part of the textile, e.g. on the should pads of a shirt or the front of a t-shirt. A metallic plate shields the user from the electronic components of the patch antenna. Because the properties of patch antennas are well known, it requires very little engineering and is thus cheap. However, integration with the textile is far from seamless, as it is very apparent to the user that he has become a giant walking antenna. Our project thus strives to find antenna designs that have emission properties as flexible as a patch antenna's while improving textile integration as to make it become transparent to the user.

The concept of a fibre-antenna rapidly established itself as an ideal solution in the research group. It provides a rich architecture upon which to build. Moreover, it can easily be spun into textile as it can loaded into the spools that deliver threads to looms. Its mechanical properties make it fit for daily use as it can resist a trip in the washing machine. Integration of the electronic components inside that fibre serves to shield both the user and the components.

3.3.1 Leaky Coaxial Cable

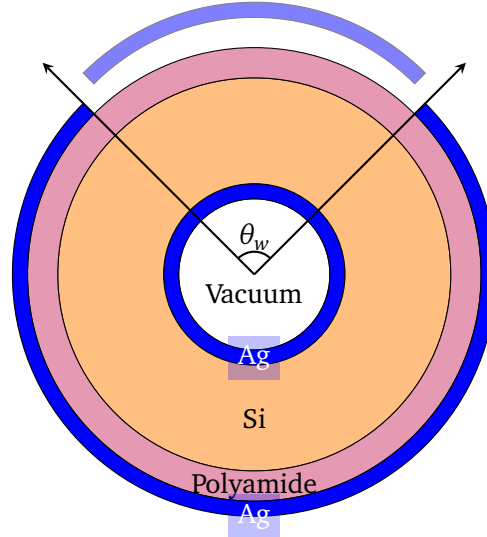
The first design we have looked into is a well known one: the *leaky coaxial fibre* (LCXF). It simply consists of a coaxial cable (metal rod, dielectric layer, metal coating) from which we have removed some of the metallic coating. These holes in the metallic coating are called “windows” and allow light to escape the confines of the coax cable, hence the moniker *leaky*. In the following section, we will look at several methods that we used to model the device and present the design parameters that were used.

Specifications of the Devices

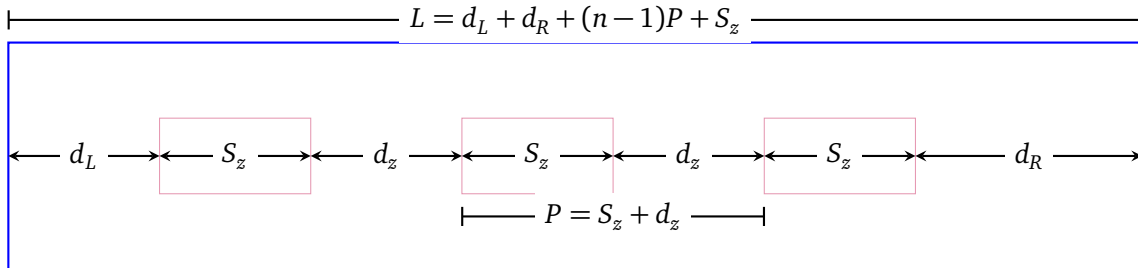
An image is worth a thousand words. Figure 3.3(a) shows a cross-section of the fibre. Figure 3.3(b) shows a top view of the antenna and display the positions of the windows. Multiple designs have been fabricated, but we retain only those that we have tried to simulate. Table 3.1a shows the actual geometrical parameters of the fibre-antennas.

On the thickness of the silver shells The thicknesses of the dilectric materials are provided by the manufacturer, Polymicro Technologies, safe for the thicknesses of the silver layers. For the time being, we have calculated those thicknesses by measuring the DC resistance of the inner and outer layers of silver and using the relation [34, p. 204]

$$R = \frac{L}{\sigma A} \tag{3.23}$$



(a) View of the cross-section: in order of increasing radius, we have: vacuum, silver, silica, polyamide and silver. We have shown a cross-section where there is a “window”. When there are no windows, the outer silver layer takes up the entire circumference of the fiber. θ_w is the angular size of the windows.



(b) Top view: the positions of the windows are usually asymmetric, i.e. $d_L \neq d_R$. The distance between the windows is given by d_z and the length of the windows are S_z . We notice that the length of the fibre is given by $L = d_L + d_R + (n - 1)P + S_z$ where $P = S_z + d_z$ is the period between windows and n is the number of windows.

Figure 3.3 – Geometry of the fibre-antenna

where L is the length of the fibre, σ the conductivity of the silver layer and A its area. For the inner and outer layers, we have

$$A_{\text{inner}} = \int_0^{2\pi} \int_{t_{\text{vac}}}^{t_{\text{vac}}+t_{\text{Ag1}}} r dr d\theta = \pi (2t_{\text{vac}}t_{\text{Ag1}} + t_{\text{Ag1}}^2) \quad (3.24)$$

$$A_{\text{outer}} = \int_0^{2\pi} \int_T^{T+t_{\text{Ag2}}} r dr d\theta = \pi (2Tt_{\text{Ag2}} + t_{\text{Ag2}}^2) \quad (3.25)$$

where $T = t_{\text{vac}} + t_{\text{Ag1}} + t_{\text{Si}} + t_{\text{pyamide}}$. Substituting these results into (3.23) yields

$$t_{\text{Ag1}}^2 + 2t_{\text{vac}}t_{\text{Ag1}} - \frac{L}{\sigma_{\text{Ag0}}\pi R_{\text{inner}}} = 0 \quad (3.26a)$$

$$t_{\text{Ag2}}^2 + 2Tt_{\text{Ag2}} - \frac{L}{\sigma_{\text{Ag0}}\pi R_{\text{outer}}} = 0 \quad (3.26b)$$

where the R s are the measured D.C. resistances measured for each shell. This can readily be solved using the quadratic equation. Using the bulk conductivity of silver (see Table 3.1b) yields the thicknesses found in Table 3.1a.

In our previous simulations, it was clear that something was amiss: there was no correlation between the simulation and experimental data. AFM pictures (see Figure 3.4) have suggested that the deposited metal is in fact a mixture of silver and silver oxide. To evaluate the effective conductivity of the mixture, we have used Bruggeman's model [35]. The model starts from a homogeneous medium, call it medium 1, of conductivity σ_1 and replaces spherical portions of this material by another one of conductivity σ_2 . When this process is done, we are left with an inhomogeneous material with partial concentrations δ_i of each material. The effective conductivity σ_e of the medium can be computed using the relation (for an arbitrary number of materials)

$$\sum_i^n \delta_i \frac{\sigma_i - \sigma_e}{\sigma_i + (d-1)\sigma_e} = 0 \quad (3.27)$$

where $\sum_i \delta_i = 1$ and d is the dimensionality of the system. Solving for σ_e in the case $n = 2$ yields

$$(d-1)\sigma_e^2 + [(d\delta_1-1)\sigma_1 + (d\delta_2-1)\sigma_2] + \sigma_1\sigma_2 = 0. \quad (3.28)$$

The positive solution is, defining $q = (d\delta_1-1)\sigma_1 + (d\delta_2-1)\sigma_2$

$$\sigma_e = \frac{1}{2d-2} \left[q + \sqrt{q^2 + 4(d-1)\sigma_1\sigma_2} \right]. \quad (3.29)$$

Size Effects It has recently come to our attention that the conductivity of thin metal films can be a function of their thicknesses. We will explore this in future work, so for now suffice it to say that the Fuchs-Sondheimer model states that

$$\sigma_F = \frac{\sigma_0}{1 + \frac{3\lambda}{8d}(1-p)} \quad (3.30)$$

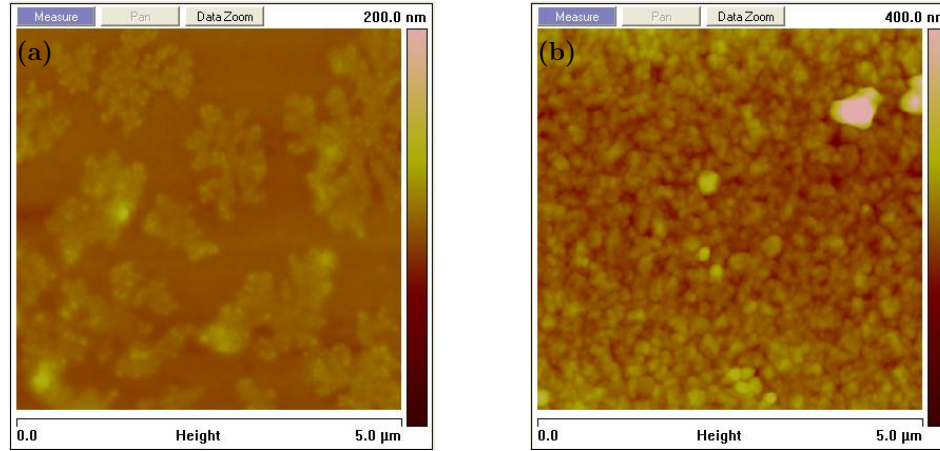


Figure 3.4 – AFM pictures of silver deposited onto glass plates. **(a)** Flakes of silver oxide seem to be forming onto the deposited silver layer. **(b)** Sample image showing the inhomogeneity of the silver layer.

where $0 \leq p \leq 1$ is a specularity parameter and λ is the electron free mean path in the metal. This model states that conductivity diminishes as the thickness of the metallic layer gets smaller.

In Figure 3.5, we compare the thicknesses obtained via the bulk conductivity model (Bruggeman effective conductivity) and the Fuchs-Sondheimer model with effective conductivity for the RF33 fibre. Given that the AFM pictures show surface inhomogeneity, we assume diffuse scattering in the FS model ($p = 0$). We see that choosing a dimensionality of 3 or 2 does not significantly affect the thicknesses, but we see a difference of about 20% in the effective conductivities.

The most interesting thing, though, is that the FS model predicts metallic layers that are 10% to 80% thicker than with the bulk conductivity model. This will be explored in the next report.

Finite Element Method

As finite element methods directly solve Maxwell’s equations, they can be a useful tool to verify semi-analytical methods. In the last report, we reported some agreement issues between experimental and simulation data. We purported that the discrepancy was due to the small size of the silver layers that we could properly account for in the finite element model. This issue has been solved by abandoning the idea of properly meshing the silver layers and replacing them by appropriate impedance boundary conditions. From HFSS’s documentation, we see that the “Layered Impedance Boundary Conditions” module follows the theory set forth in [36] and others.

We have simulated the RF21 fibre using Bruggeman’s model for the effective conductivity and with values of $\delta_1 \in \{0, 1\}$ and $d = 3$ in (3.29). After obtaining the simulated S_{11} parameter of the fibre, we compared it to the experimentally obtained one using the Pearson correlation coefficient.

Table 3.1 – Units are repeated from column above if not indicated.

a Geometric parameters of the RF21/RF33 fibre designs. The thicknesses of the layers are listed in order, stating from the inner layer to the outer layer of the fibre-antenna.

Quantity	Unit	RF21	RF33
t_{vac}	μm	99.874	99.924
t_{Ag1}		0.126	0.0766
t_{Si}		273	273
t_{pyamide}		24	24
t_{Ag2}		0.101	0.030
d_L	mm	27	30.91
d_R		55	54.72
S_{z1}^1		32	34.36
S_{z2}		32	34.06
S_{z3}		32	33.87
d_{z1}		28	27.44
d_{z2}		28	28.36
L	cm	30.0	24.372
θ_w	deg	180	180
R_{inner}	Ω	60.0	80.5
R_{outer}		20.0	59.8

b Physical parameters of the materials used in the RF21/RF33 antennas.

Quantity	Unit	Value
ϵ_{Si}	–	3.77
$\epsilon_{\text{pyamide}}$	–	3.50
σ_{Ag0}	MS/m	63.0
σ_{AgO0}		6.79
λ_{Ag}	nm	40

¹ Each window has a different S_z and d_z .

For two samples $\{X_i\}$ and $\{Y_i\}$, it is defined as

$$r = \frac{\sum_i^n (X_i - \langle X \rangle)(Y_i - \langle Y \rangle)}{\sqrt{\sum_i^n (X_i - \langle X \rangle)^2} \sqrt{\sum_i^n (Y_i - \langle Y \rangle)^2}}. \quad (3.31)$$

From the definition, we see that the simultaneous linear transformations $X_i \rightarrow b + aX_i$ and $Y_i \rightarrow d + cY_i$ do not change the value of the Pearson coefficient. This means that even if the two samples do not have the same normalization or are shifted by a constant amount, the correlation will stay the same. As such, the Pearson correlation measures the `delegend(loc=1, prop='size':6)` gree at which both samples are linearly related.

Figure 3.6 shows the experimental and simulated S_{11} parameter. At first look, it might seem like the general form of the curves are similar, but our quantitative analysis will show that that would be wrong. To make sure that our simulation data was not simply shifted in frequency due to an small error in the geometry, we have also calculated the correlation for a shifted dataset . This changes the Pearson correlation because we must elide some of the experimental and simulation data to do so. Figure 3.7 shows our results. We see that there are little to no correlation between the simulation data and the experimental data with $r \in \{-0.04, 0.05\}$.

To do so, we simply right-shifted the arrays containing the simulation data and removed the data that fell outside the frequency range of the experimental data.

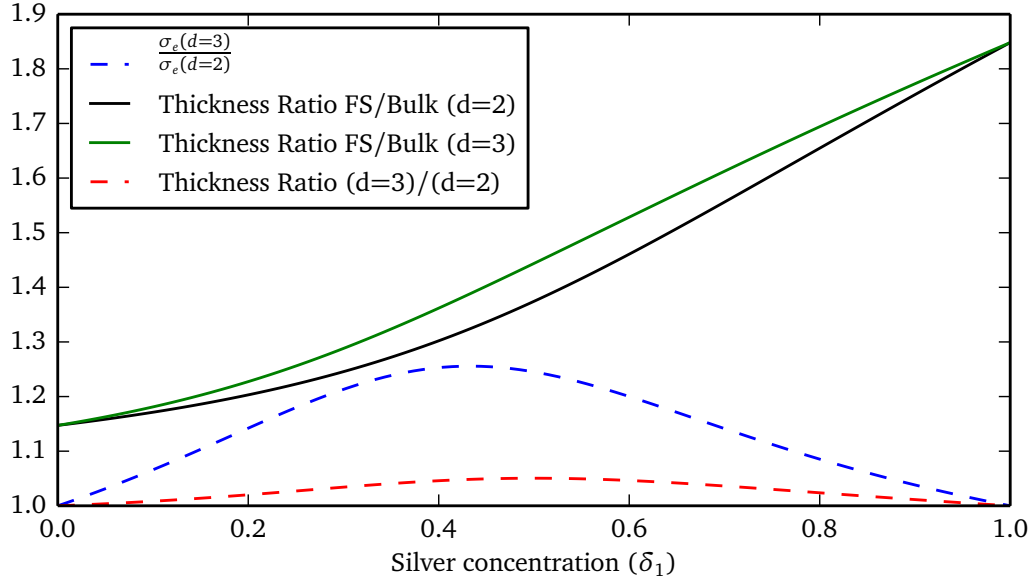


Figure 3.5 – We show multiple ratios as a function of the silver concentration, δ_1 . The blue line shows the ratio between the effective conductivities for a choice of $d = 2$ and $d = 3$. The black and green lines show the ratio of the thickness predicted by using the Fuchs-Sondheimer conductivity in Eq. (3.26) to the thickness predicted by using the bulk conductivity. The red line shows the ratio of the green line to the black line.

A possible source of error is the thickness of the silver layers. We will incorporate the FS model in the next simulations and determine if it is a factor.

We have also taken the Fourier transform of the experimental and simulation data (for $\delta_1 = 0$). To our discontent, it seems that the datasets do not share periodic properties. Figure 3.8 shows the intensity of the FFT transform. To see if the periodic components corresponded to particular lengths in the system, we converted the associated wavelengths to frequencies and plotted them as vertical lines in the figure. f_1 is the fundamental mode of infinite LCXF, namely

$$f_1 = \frac{c}{(S_z + d_z)(\sqrt{\epsilon_{Si}} + 1)}. \quad (3.32)$$

The frequency associated with the optical and the actual lengths of the window are

$$l_{\text{opt}} = \frac{c}{S_z \sqrt{\epsilon_{Si}}}$$

$$l_{\text{phy}} = \frac{c}{S_z}.$$

Nothing thus far seems to explain the periodic properties of the S_{11} parameter of the experimental and simulation, although the optical length of the windows seems to explain a single peak in the Fourier power spectrum.

The author is not sure that is the proper method to analyze the Fourier spectrum, however.

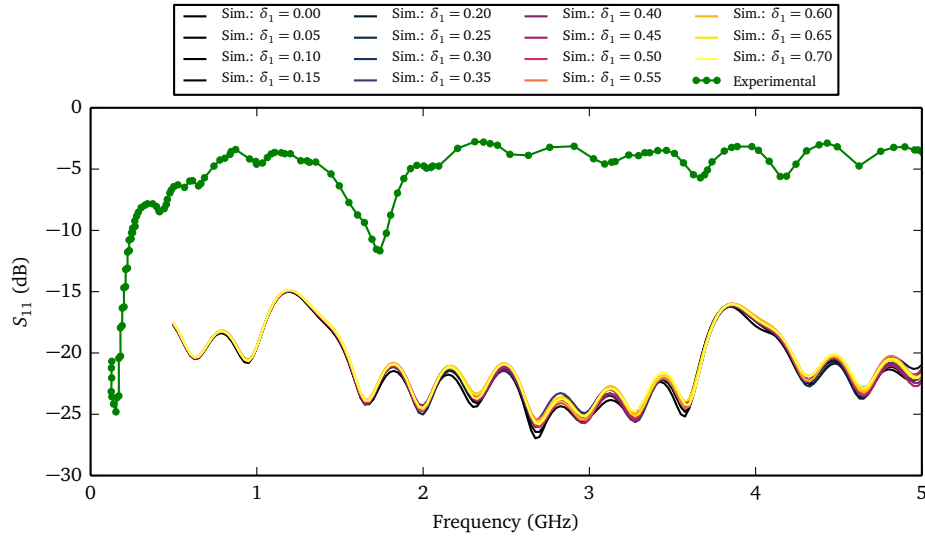


Figure 3.6 – Experimental and simulated S_{11} parameter for the RF21 fibre.

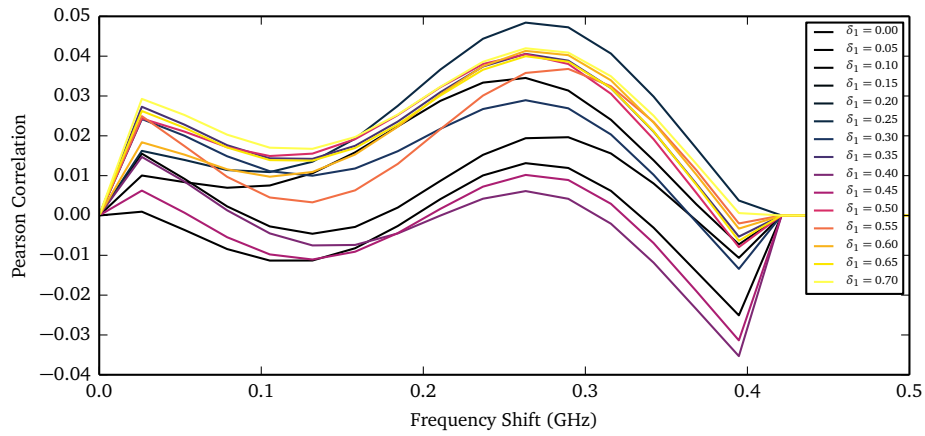


Figure 3.7 – Pearson correlation coefficient as a function of the frequency shift of the data.

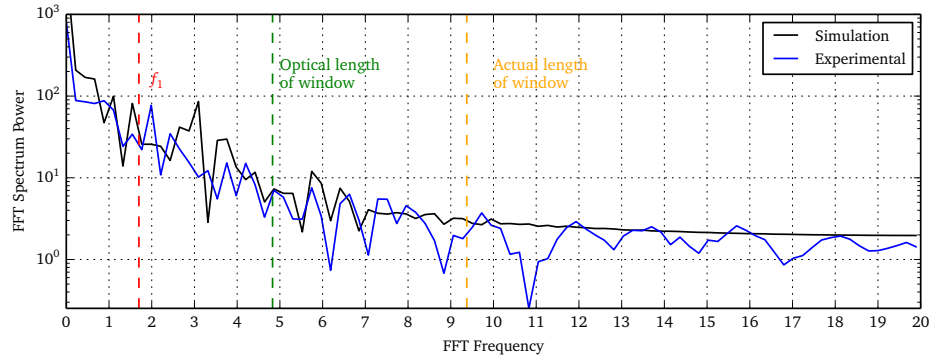


Figure 3.8 – Absolute value of the Fourier transform of the S_{11} parameter. The red lines denote the frequencies associated with certain lengths in the RF21 fibre design.

Chapter 4

Conclusion

Appendix A

Bessel Functions

This appendix contains some results concerning the Bessel functions. Given our reduction of Maxwell's equations from 3D to 2D using cylindrical coordinates, the Bessel functions will form the basis of our analysis, as the Bessel functions are the eigenfunctions of Helmholtz's equation in those coordinates.

We thus wish to collect some of their most important properties here for easy reference. Most of them come from the celebrated volume by Abramowitz & Stegun [37], while a few come from [38]. Proper reference will be given.

In what follows, $\nu, z \in \mathbb{C}$ and $n \in \mathbb{N}$ unless explicitly stated otherwise.

A.1 Definition and Elementary Properties

A.1.1 Differential Equation

The Bessel functions solve the differential equation

$$z^2 \frac{d^2 w}{dz^2} + z \frac{dw}{dz} + (z^2 - \nu^2)w = 0 \quad (\text{A.1})$$

which is a special case of the confluent hypergeometric differential equation, which is in turn a special case of the hypergeometric differential equation. When solved via Fröbenius' method, it yields the solution

$$J_\nu(z) = \sum_{k=0}^{\infty} \frac{(-1)^k \left(\frac{1}{2}z\right)^{\nu+2k}}{k! \Gamma(\nu + k + 1)}. \quad (\text{A.2})$$

This is the Bessel function of the first kind. A second, linearly independent is defined by

$$Y_\nu(z) = \frac{J_\nu(z) \cos \pi \nu - J_{-\nu}(z)}{\sin \pi \nu} \quad (\text{A.3})$$

where a valid limiting process must be used when $\nu \rightarrow n$.

We will be mostly interested in a second set of linearly independent solutions: the Hankel functions. They are defined by

$$H_\nu^{(+)}(z) = J_\nu(z) + iY_\nu(z) \quad (\text{A.4a})$$

$$H_\nu^{(-)}(z) = J_\nu(z) - iY_\nu(z). \quad (\text{A.4b})$$

We will alternatively use the notation

$$H_\nu^{(\omega)} = J_\nu(z) + i\omega Y_\nu(z) \quad (\omega = \pm) \quad (\text{A.5})$$

to describe both functions at the same time.

A.1.2 Recurrence Relations

From the differential equation itself, we can derive multiple recurrence relations that the whole family of Bessel functions obey. If \mathcal{C} denotes J , Y , $H^{(\pm)}$ or any linear combination of the four functions, we have

$$\mathcal{C}_{\nu-1}(z) + \mathcal{C}_{\nu+1}(z) = \frac{2\nu}{z} \mathcal{C}_\nu(z) \quad (\text{A.6a})$$

$$\mathcal{C}_{\nu-1}(z) - \mathcal{C}_{\nu+1}(z) = 2\mathcal{C}'_\nu(z) \quad (\text{A.6b})$$

$$\mathcal{C}_{\nu-1}(z) - \frac{\nu}{z} \mathcal{C}_\nu(z) = \mathcal{C}'_\nu(z) \quad (\text{A.6c})$$

$$-\mathcal{C}_{\nu+1}(z) + \frac{\nu}{z} \mathcal{C}_\nu(z) = \mathcal{C}'_\nu(z). \quad (\text{A.6d})$$

However, the minimal solution to these recurrence relations is $J_\nu(z)$, so any attempt at numerically evaluating Y or $H_\nu^{(\pm)}$ using these is foiled (see §C.2 for details).

A.1.3 Relations between Solutions

The following are analytical relationships between the set of Bessel functions. They can be of use in both standard and numerical analysis.

Reflection Formulas [39, p. 286]

$$J_{-\nu}(z) = \cos \nu\pi J_\nu(z) - \sin \nu\pi Y_\nu(z) \quad (\text{A.7a})$$

$$Y_{-\nu}(z) = \sin \nu\pi J_\nu(z) + \cos \nu\pi Y_\nu(z) \quad (\text{A.7b})$$

$$J_{-n}(z) = (-1)^n J_n(z) \quad (\text{A.7c})$$

$$Y_{-n}(z) = (-1)^n Y_n(z) \quad (\text{A.7d})$$

$$H_{-\nu}^{(\omega)} = e^{i\omega\nu\pi} H_\nu^{(\omega)} \quad (\text{A.7e})$$

Complex Conjugate ($\nu \in \mathbb{R}$)

$$\overline{J_\nu(z)} = J_\nu(\bar{z}) \quad (\text{A.8a})$$

$$\overline{Y_\nu(z)} = Y_\nu(\bar{z}) \quad (\text{A.8b})$$

$$\overline{H_\nu^\omega(z)} = H_\nu^{(-\omega)}(\bar{z}) \quad (\text{A.8c})$$

A.2 Asymptotic and Limiting Forms

A.2.1 Expansions for Small Arguments and Fixed ν

From the first few terms of the power series (A.1),

$$J_\nu(z) = \frac{1}{\Gamma(\nu+1)} \left(\frac{z}{2}\right)^\nu \left[1 - \frac{1}{\nu+1} \left(\frac{z}{2}\right)^2\right] + \mathcal{O}(z^{\nu+4}). \quad (\text{A.9})$$

Using the first terms of the ascending series [37, §9.1.11]

$$\begin{aligned} Y_n(z) = & -\frac{1}{\pi} \left(\frac{z}{2}\right)^{-n} \sum_{k=0}^{n-1} \frac{(n-k-1)!}{k!} \left(\frac{z}{2}\right)^{2k} + \frac{2}{\pi} \ln \frac{z}{2} J_n(z) \\ & - \frac{1}{\pi} \left(\frac{z}{2}\right)^n \sum_{k=0}^{\infty} \{\psi(k+1) + \psi(n+k+1)\} \left(\frac{z}{2}\right)^{2k} \frac{1}{k!(n+k)!}, \end{aligned} \quad (\text{A.10})$$

where

$$\psi(n+1) = -\gamma + \sum_{k=1}^n k^{-1} \quad (\gamma = 0.57721\,56649\dots) \quad (\text{A.11})$$

is the digamma function. The cases $n = 0$ and $n \neq 0$ differ

$$Y_0(z) = \frac{2}{\pi} \left(\ln \frac{z}{2} + \gamma\right) + \mathcal{O}(z^2) \quad (\text{A.12})$$

$$Y_n(z) = -\frac{(n-1)!}{\pi} \left(\frac{z}{2}\right)^{-n} + \mathcal{O}(z^{-n+2}). \quad (\text{A.13})$$

The expansions of the Hankel functions is found by using their definition (A.4):

$$H_0^{(\omega)}(z) = 1 + \frac{2i\omega}{\pi} \left(\ln \frac{z}{2} + \gamma\right) + \mathcal{O}(z^2) \quad (\text{A.14})$$

$$H_n^{(\omega)}(z) = -\frac{i\omega(m-1)!}{\pi} \left(\frac{z}{2}\right)^{-n} + \mathcal{O}(z^{-n+2}). \quad (\text{A.15})$$

A.2.2 Expansions for Large Arguments and Fixed ν

The Bessel functions, jealous of the simpler trigonometric functions, try to mimic them when their arguments get large. We have

$$J_\nu(z) \approx \sqrt{\frac{2}{\pi z}} \cos\left(z - \frac{\nu\pi}{2} - \frac{\pi}{4}\right) \quad (\text{A.16a})$$

$$Y_\nu(z) \approx \sqrt{\frac{2}{\pi z}} \sin\left(z - \frac{\nu\pi}{2} - \frac{\pi}{4}\right) \quad (\text{A.16b})$$

$$H_\nu^{(\omega)}(z) \approx \sqrt{\frac{2}{\pi z}} e^{i\omega\left(z - \frac{\nu\pi}{2} - \frac{\pi}{4}\right)} \quad (\text{A.16c})$$

Appendix B

Basic Equations of Bidimensional Cavities

B.1 SALT Equations for TE and TM Polarizations

B.2 Specialization to Dielectric Cavities

Appendix C

Numerical Tools

C.1 Numerical Computation of the Scattering Matrix

C.2 Computation of the Logarithmic Derivative $[H_\nu^{(\pm)}(z)]'/H_\nu^{(\pm)}(z)$

As we have seen from Appendix B, the computation of the logarithmic derivative of Bessel functions is of the utmost importance in the numerical solution of scattering problems. Given that we already use Amos' library to evaluate the Bessel functions, we might have been tempted to use it to directly evaluate the derivative. It turns out that using expansions that pertain to logarithmic derivatives is somewhat faster and is more accurate than using Amos' library.

In this section, we introduce some concepts relating to continued fraction expansions (CFEs) and discuss their numerical evaluation. We then derive the CFEs and other expansions that will be of use in the computation of the logarithmic derivatives.

C.2.1 Notation and Necessary Theorems

A continued fraction expansion is a representation of a mathematical function. It can be linked to Laurent series, Padé approximants and much more [38]. It has the standard form

$$f = b_0 + \frac{a_1}{b_1 + \frac{a_2}{b_2 + \frac{a_3}{b_3 + \frac{a_4}{b_4 + \dots}}}} \quad (\text{C.1})$$

or, more succinctly,

$$f = b_0 + \mathbf{K}_{m=1}^{\infty} \left(\frac{a_m}{b_m} \right) \quad (\text{C.2})$$

where 'K' is for the German word *Kettenbruch*, meaning continued fraction. We define the n th approximant as

$$f_n = b_0 + \mathbf{K}_{m=1}^n \left(\frac{a_m}{b_m} \right). \quad (\text{C.3})$$

We will be concerned with their numerical evaluation and convergence properties.

Notice that naïvely evaluating the CFE from right-to-left, as a person would do, does not yield a satisfying numerical algorithm, as the amount of iterations must be fixed in advance and consequently does not allow the control the accuracy of the evaluation. The chosen method is taken from the Holy Bible of Numerics, *Numerical Recipes* [39] and is called the modified Lentz's method. It constructs a rational approximation of the n th approximant

$$f_n = \frac{A_n}{B_n} \quad (\text{C.4})$$

where

$$\begin{aligned} A_{-1} &= 1 & B_{-1} &= 0 \\ A_0 &= b_0 & B_0 &= 1 \\ A_j &= b_j A_{j-1} + a_j A_{j-2} & B_j &= b_j B_{j-1} + a_j B_{j-2}. \end{aligned} \quad (\text{C.5})$$

This method can lead to over/underflow of the floating-point representation: the method hence uses

$$\begin{aligned} C_j &= A_j / A_{j-1} & D_j &= B_{j-1} / B_j \\ &= b_j + \frac{a_j}{C_{j-1}} & &= \frac{1}{b_j + a_j D_{j-1}} \\ f_j &= f_{j-1} C_j D_j. \end{aligned} \quad (\text{C.6})$$

The method is aptly described by Algorithm 1. It allows for a left-to-right evaluation of the CFE and control of the relative accuracy of the computation.

As for the convergence properties, we will only bother with CFEs originating from three-term recurrence relations. Indeed, it turns out that any three-term recurrence relation can be linked to a CFE. Consider

$$y_{n+1} + a_n y_n + b_n y_{n-1} = 0. \quad (\text{C.7})$$

It can be rewritten as

$$\frac{y_n}{y_{n-1}} = -\frac{b_n}{a_n + y_{n+1}/y_n}. \quad (\text{C.8})$$

Iterating yields the CFE

$$\frac{y_n}{y_{n-1}} = \mathbf{K}_{m=n}^{\infty} \left(\frac{-b_m}{a_m} \right). \quad (\text{C.9})$$

Given our goal of computing $[H_\nu^{(\pm)}(z)]' / H_\nu^{(\pm)}(z)$ and in light of (ref to recurrence relation of Bessel functions), it seems that we have won. The next theorem, however, will prove us wrong.

Algorithm 1: Evaluation of Continued Fractions**Data:** tiny = square root of smallest representable number**Data:** eps = accuracy of the CFE**if** $b_0 = 0$ **then**| $f_0 \leftarrow \text{tiny}$ **else**| $f_0 \leftarrow 0$ $C_0 \leftarrow f_0;$ $D_0 \leftarrow 0;$ **repeat** from $j = 1$ | $D_j \leftarrow b_j + a_j D_{j-1};$ | **if** $D_j = 0$ **then**| | $D_j \leftarrow \text{tiny}$ | $C_j \leftarrow b_j + \frac{a_j}{C_{j-1}};$ | **if** $C_j = 0$ **then**| | $C_j \leftarrow \text{tiny}$ | $D_j \leftarrow 1/D_j;$ | $\Delta_j \leftarrow C_j D_j;$ | $f_j \leftarrow f_{j-1} \Delta_j$ **until** $|\Delta_j - 1| < \text{eps};$ **return** f_j

Theorem C.1 (Pincherle's Theorem [38]). *If there exists a minimal solution u_n of the three-term recurrence relation (C.7), the associated CFE (C.9) converges to u_n/u_{n-1} . A solution is said minimal if there exists another solution v_n such that*

$$\lim_{n \rightarrow \infty} \frac{u_n}{v_n} = 0. \quad (\text{C.10})$$

v_n is said to be the dominant solution. The minimal solution is unique.

Because the minimal solution of (A.6a) is $J_\nu(z)$, we cannot use the associated CFE to compute the logarithmic derivatives of Hankel functions. Instead, we must look into the links between Hankel functions and confluent hypergeometric functions.

C.2.2 CFE and Other Expansions

In this brief foray into the vast subject of hypergeometric functions, we will introduce Kummer's function and its link to the evaluation of the logarithmic derivative.

Kummer's function solves the differential equation [37, §13.1.1]

$$z \frac{d^2 y}{dz^2} + (b - z) \frac{dy}{dz} - ay = 0 \quad (\text{C.11})$$

and is noted $U(a, b, z)$. It can be shown that that $u_k = (a)_k U(a + k, b, z)$ is the minimal solution of the recurrence [40]

$$u_{n+1} = \frac{2a - b + 2n + z}{a - b + n + 1} u_n - \frac{a + n - 1}{a - b + n + 1} u_{n-1} \quad (\text{C.12})$$

where $(a)_k$ is the Pochhammer symbol. We can hence derive

$$\frac{U(a, b, z)}{U(a + 1, b, z)} = 2a - b + 2 + z - \prod_{m=1}^{\infty} \left(\frac{(a + m)(b - a - m - 1)}{b - 2a - 2m - 2 - z} \right). \quad (\text{C.13})$$

Combined with [37, §13.4.23]

$$U(a + 1, b, z) = \frac{1}{1 + a - b} U(a, b, z) + \frac{z}{a(1 + a - b)} U'(a, b, z), \quad (\text{C.14})$$

we obtain [38]

$$\frac{dU(a, b, z)/dz}{U(a, b, z)} = -\frac{a}{z} + \frac{a(1 + a - b)/z}{2a - b + 2 + z} - \prod_{m=1}^{\infty} \left(\frac{(a + m)(b - a - m - 1)}{b - 2a - 2m - 2 - z} \right). \quad (\text{C.15})$$

Given the relation between Kummer's functions and Hankel functions $H_\nu^\omega(z)$ [37, §13.6.22/23]

$$H_\nu^\omega(z) = \frac{2}{\sqrt{\pi}} e^{-\omega[\pi(\nu+1/2)-z]} (2z)^\nu U(\nu + 1/2, 2\nu + 1, -2i\omega z) \quad (\omega = \pm) \quad (\text{C.16})$$

we can finally find the CFE

$$\frac{dH_\nu^\omega(z)/dz}{H_\nu^\omega(z)} = -\frac{1}{2z} + i\omega + \frac{\omega}{z} \prod_{m=1}^{\infty} \left(\frac{\nu^2 - (2m - 1)^2/4}{2(iz - \omega m)} \right). \quad (\text{C.17})$$

In our numerical implementation (see next section), we have found that when $|z| < 10^{-2}$, convergence is slow. This mirrors the results of [41]. We thus use the small argument expansions for the Bessel functions (q.v. §A.2.1) to obtain

$$\lim_{z \rightarrow 0} \frac{dH_\nu^\omega(z)/dz}{H_\nu^\omega(z)} = -\frac{\nu}{z} \quad (\nu \neq 0) \quad (\text{C.18a})$$

$$= \frac{1}{z} \left[\frac{\pi}{2i\omega} + \gamma + \ln\left(\frac{z}{2}\right) \right]^{-1} \quad (\nu = 0). \quad (\text{C.18b})$$

C.2.3 Numerical Tests

We have performed a number of tests to ascertain the performance of our algorithm. To test the precision of the algorithm, we have evaluated the CFE for $z \in \{0, 10\}$ and $\nu \in \{-100, 100\} \in \mathbb{N}$ and compared it to the values obtained via Amos' library for a range of tolerances. It can be seen that the maximum deviation decreases until our set tolerance hits 10^{-12} and then plateaus. Because convergence of C.17 is mathematically insured, we conclude that Amos's library evaluate the logarithmic derivative up to a precision of 10^{-12} . This is probably due to the propagation of errors in the floating point operations, as we use relation (A.6b) to evaluate the derivative.

However, it can be seen that Amos' library is somewhat faster, given its precision, that our CFE evaluation even though it requires three Hankel function evaluations.

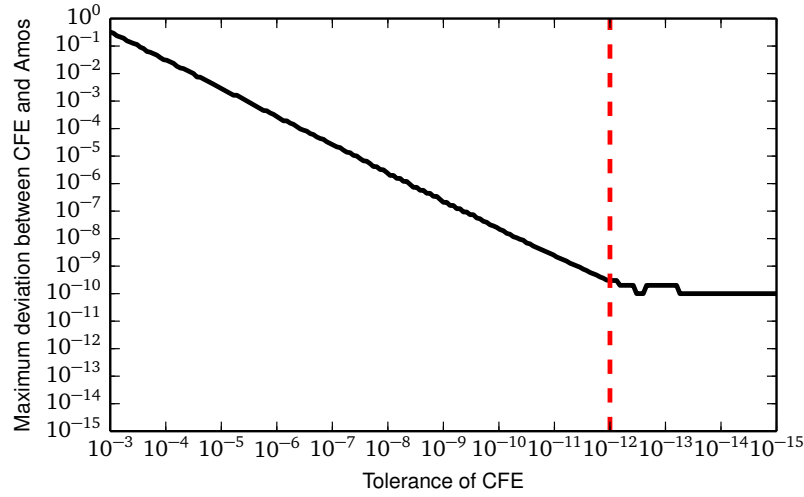
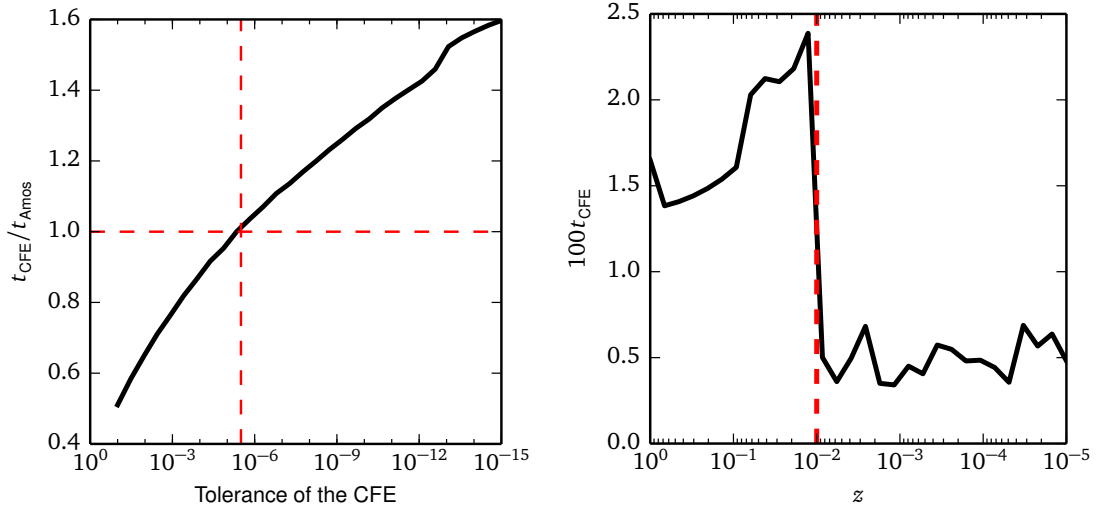


Figure C.1 – Maximum deviation between the CFE and Amos' implementation of the Bessel functions as a function of the tolerance of the CFE. This study was performed in the parameter space $z \in \{0.1, 10\}$, $\nu \in \{-100, 100\}$. We interpret the plateau in maximum deviation as the error committed by Amos' implementation, i.e. Amos' implementation has a precision of $\sim 10^{-10}$ on the evaluation of the logarithmic derivative.



(a) Performance of the CFE implementation as a function of its tolerance. We measured the ratio of the time it takes to compute the logarithmic derivative at $z = 0$ for all orders $\nu \in \{-100, 100\}$ with the CFE and Amos' implementation. When the tolerance of the CFE hits $\sim 10^{-5.5}$, the CFE is slower than Amos' implementation.

(b) Performance of the CFE as a function of z . When approaching $z = 0$ (from all sides), it takes a higher number of terms for the CFE to converge, resulting in a slower algorithm. However, at $z = 10^{-2}$, we use the small argument form, preserving both precision and performance.

Figure C.2 – Performance of the CFE compared to that of Amos' library. The CFE is somewhat slower, but can achieve better precision.

C.3 Wigner Symbols

Before discussing the Wigner symbols, we introduce the Clebsch-Gordan coefficients as they appear quite naturally in the quantum theory of angular momentum. Specifically, they are needed to study the coupling of two systems having definite angular momenta. The material in this section is inspired by [42, 43].

C.3.1 Formal definitions

Clebsch-Gordan coefficients and Wigner $3j$ -symbols

Given two states that can be described by two quantum numbers pertaining to their angular momenta, say $|j_1 m_1\rangle$ and $|j_2 m_2\rangle$ where j_1 and j_2 are the total angular momenta and m_1 and m_2 are their z -projections. The states span two different vectors spaces, ξ_1 and ξ_2 . To measure the angular momentum and associated z -projection of the composite system, call them j_3 and m_3 , we look at the states spanning the product space $\xi_1 \otimes \xi_2$. The product states can be written

$$|j_3 m_3\rangle = \sum_{m_1} \sum_{m_2} |j_1 m_1 j_2 m_2\rangle \langle j_1 m_1 j_2 m_2 | j_3 m_3\rangle \quad (\text{C.19})$$

where

$$|j_1 m_1 j_2 m_2\rangle = |j_1 m_1\rangle \otimes |j_2 m_2\rangle$$

and where the allowed values of j_3 and m_3 follow from the quantum vector addition rules.

A similar relation holds for the bra. This equation simply describes the expansion of the a vector in the product space $\xi_1 \otimes \xi_2$ in the product of the bases of ξ_1 and ξ_2 [44]. The expansion coefficients are known as the Clebsch-Gordan coefficients. Their square represent the probability that a measurement of the angular momentum yields a value of $\sqrt{j_3(j_3 + 1)}\hbar$.

We will note the Clebsch-Gordan coefficients as

$$C_{j_1 m_1, j_2 m_2}^{j_3 m_3} = \langle j_1 m_1 j_2 m_2 | j_3 m_3\rangle. \quad (\text{C.20})$$

We can now introduce the Wigner $3j$ -symbols. They can be related to the Clebsch-Gordan coefficients through

$$\begin{pmatrix} j_1 & j_2 & j_3 \\ m_1 & m_2 & m_3 \end{pmatrix} = \frac{(-1)^{j_1 - j_2 - m_3}}{\sqrt{2j_3 + 1}} \langle j_1 m_1 j_2 m_2 | j_3 - m_3\rangle. \quad (\text{C.21})$$

More telling, though, is their interpretation as the probability that three angular momenta couple to give zero angular momentum, or

$$\begin{pmatrix} j_1 & j_2 & j_3 \\ m_1 & m_2 & m_3 \end{pmatrix} = (-1)^{j_1 - j_2 + j_3} \sum_{j' m'} C_{j_1 m_1, j_2 m_2}^{j' m'} C_{j' m', j_3 m_3}^{00}. \quad (\text{C.22})$$

The 3j-symbols also appear in the angular integration of three spherical harmonics

$$\iint_{\Omega} Y_{j_1, m_1}(\theta, \varphi) Y_{j_2, m_2}(\theta, \varphi) Y_{j_3, m_3}(\theta, \varphi) d\Omega = \sqrt{\frac{(2j_1+1)(2j_2+1)(2j_3+1)}{4\pi}} \begin{pmatrix} j_1 & j_2 & j_3 \\ 0 & 0 & 0 \end{pmatrix} \begin{pmatrix} j_1 & j_2 & j_3 \\ m_1 & m_2 & m_3 \end{pmatrix} \quad (\text{C.23})$$

Wigner 6j-symbols

The 6j-symbols are related to the coupling of three angular momenta. In this case, the resultant angular momentum \mathbf{j} can be obtained via three different coupling schemes:

- I. $\mathbf{j}_1 + \mathbf{j}_2 = \mathbf{j}_{12}, \quad \mathbf{j}_{12} + \mathbf{j}_3 = \mathbf{j};$
- II. $\mathbf{j}_2 + \mathbf{j}_3 = \mathbf{j}_{23}, \quad \mathbf{j}_1 + \mathbf{j}_{23} = \mathbf{j};$
- III. $\mathbf{j}_1 + \mathbf{j}_3 = \mathbf{j}_{13}, \quad \mathbf{j}_{13} + \mathbf{j}_2 = \mathbf{j}.$

Each coupling scheme has a set of associated *generalized Clebsch-Gordan* coefficients which gives the coefficients of the expansion of a state vector in the basis of $|j_1 m_1, j_2 m_2, j_3 m_3\rangle$. For instance, a state corresponding to coupling scheme I has expansion

$$|j_1 j_2(j_{12}), j_3 j m\rangle = \sum_{m_1, m_2, m_3} C_{j_1 m_1 j_2 m_2}^{j m} C_{j_{12} m_{12} j_3 m_3}^{j m} |j_1 m_1, j_2 m_2, j_3 m_3\rangle \quad (\text{C.24})$$

with similar expressions holding for the other coupling schemes.

We thus define the 6j-symbols as the coefficients of the unitary transformation that takes us from one scheme to another [42]. We can then write

$$\left\{ \begin{matrix} j_1 & j_2 & j_3 \\ j_4 & j_5 & j_6 \end{matrix} \right\} = \frac{(-1)^{j_1+j_2+j_4+j_5}}{\sqrt{(2j_3+1)(2j_6+1)}} \sum_{m_1, m_2, m_3, m_4, m_5, m_6} C_{j_3 m_3, j_4 m_4}^{j_5 m_5} C_{j_1 m_1, j_2 m_2}^{j_3 m_3} C_{j_1 m_1, j_6 m_6}^{j_5 m_5} C_{j_2 m_2, j_4 m_4}^{j_6 m_6} \quad (\text{C.25})$$

We can also define higher-order Wigner symbols, but things rapidly become complicated [45].

C.3.2 Numerical Computation of Wigner Symbols

The previous section dealt with the definitions of the Clebsch-Gordan coefficients and the Wigner symbols. While more (much, much more) could have been said on the subject, we will now discuss the actual evaluation of these numbers.

We note that the Condon-Shortley phase convention assures us all Clebsch-Gordan coefficients and Wigner symbols are real, which is a real numerical advantage.

Moreover, there exists closed-forms formulas in the form of algebraic sums for the Wigner symbols, but they are riddled with numerical issues, such as the cancellation of large terms and the evaluation of the ratio of large factorial arguments.

The best way to evaluate the coefficient was devised in 1975 by chemical physicist K. Schulten [46]. He and R. G. Gordon rederived three-term recursion relation for the Wigner symbols and used them to evaluate sets of Wigner symbols at a time. Fortran code exists, but our tests showed only single numerical precision. We have thus reprogrammed the algorithm, first described in [46] and detailed in [47], in C++.

Before detailing our results, we will briefly overview the algorithm used (see Figure C.4. We compute

$$\begin{pmatrix} j_1 & j_2 & j_3 \\ m_1 & m_2 & m_3 \end{pmatrix} \quad \forall j_1$$

$$\begin{Bmatrix} j_1 & j_2 & j_3 \\ j_4 & j_5 & j_6 \end{Bmatrix} \quad \forall j_1$$

We can write the recursion relations valid for both symbols as (we adopt the notation of [48])

$$\alpha_\psi(j_1)\psi(j_1 + 1) + \beta_\psi(j_1)\psi(j_1) + \gamma_\psi(j_1)\psi(j_1 - 1) = 0 \quad (\text{C.26})$$

where $\psi(j_1)$ represents either the $3j$ - or $6j$ -symbol at j_1 and the Greek letters are the coefficient at that j_1 . They are shown in Table C.1.

To start the recursion, we would usually need two initial conditions. It turns out, however, that the recursion relations reduce to only two terms at the boundaries $j_{1\min}$ and $j_{1\max}$. Like all other numerical schemes, recursion relations are only stable in the direction of increasing coupling coefficients. Semi-classical analysis [46] informs us that there generally exists three regions of interest for the function $\psi(j_1)$. Near the boundaries, we are in the nonclassical regions. At the lower values of j_1 , $\psi(j_1)$ is increasing until it hits the central classical region, where it starts oscillating. On the other hand, near the $j_{1\max}$ boundaries, the coefficients are increasing with decreasing j_1 . Given the linearity of the recursion relations, we can start the recursion relations from both boundaries using a sufficiently small but otherwise *arbitrary* number. While the ratios between successive values of the coupling coefficients will be correct, their absolute values will not. The forward and backward recurrences will be multiplied by a scalar, call them c_1 for the forward recursion and d_1 for the backward recursion. To find the relationship between the scalars, we watch the values of the forward and backward recursions at some intermediary point. For more numerical stability, we use three contiguous values around the intermediary point and find the parameter $\lambda = d_1/c_1$ from a least-squares fit. To choose the intermediary point, we note that the recursion relations appear in the form

$$\psi(j_1 + 1) = X(j_1)\psi(j_1) + Y(j_1)\psi(j_1 - 1). \quad (\text{C.27})$$

Schulten found that, using semiclassical analysis, that $|X(j_1)|$ attains its minimum value in the classical domain. Monitoring the variation of $|X(j_1)|$ thus provides a way to find the intermediary point.

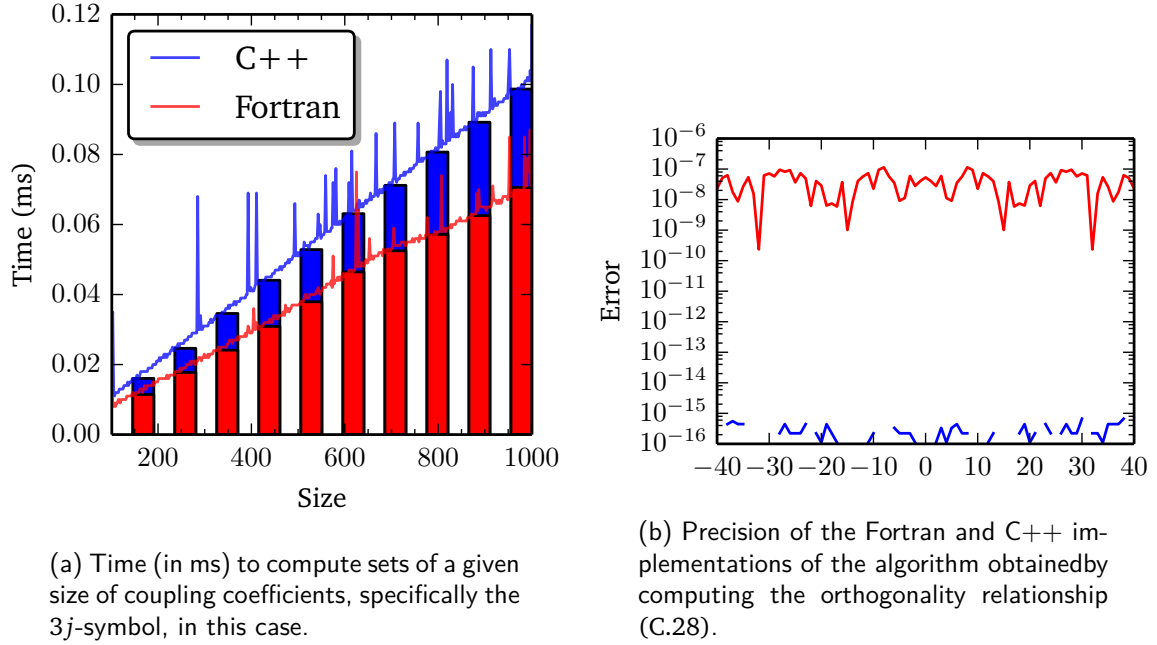


Figure C.3 – Performance and precision of our numerical algorithms.

The overall scaling factor c_1 is found and the set of coupling coefficients is rescaled to its proper value by using the normalization condition on the computed set.

We note that if the total size of the set is 1 ($j_{\min} = j_{\max}$), we can deduce, from the triangular condition, that $l_2 \vee l_3 = 0$. We thus have to evaluate the $3j$ -symbols

$$\begin{aligned} \begin{pmatrix} l_3 & 0 & l_3 \\ -m_3 & 0 & m_3 \end{pmatrix} &= \begin{pmatrix} l_3 & l_3 & 0 \\ m_3 & -m_3 & 0 \end{pmatrix} = \frac{(-1)^{l_3-m_3}}{\sqrt{2l_3+1}} \\ \begin{pmatrix} l_2 & l_2 & 0 \\ -m_2 & m_2 & 0 \end{pmatrix} &= (-1)^{-2l_2} \begin{pmatrix} l_2 & l_2 & 0 \\ m_2 & -m_2 & 0 \end{pmatrix} \\ &= \frac{(-1)^{-l_2-m_3}}{\sqrt{2l_2+1}} \end{aligned}$$

When the size is 2, we simply the two-term recursion formula with an arbitrary initial condition and normalize the two coefficients obtained.

$$\sum_{m_1, m_2} (2l_3 + 1) \begin{pmatrix} l_1 & l_2 & l_3 \\ m_1 & m_2 & m_3 \end{pmatrix}^2 = 1 \quad (\text{C.28})$$

C.4 Spherical Harmonics Transform

In the variable phase method, we must find the spherical harmonics transform, i.e. the spherical moments, of the potential. To find these moments, we will have to become intimate with the

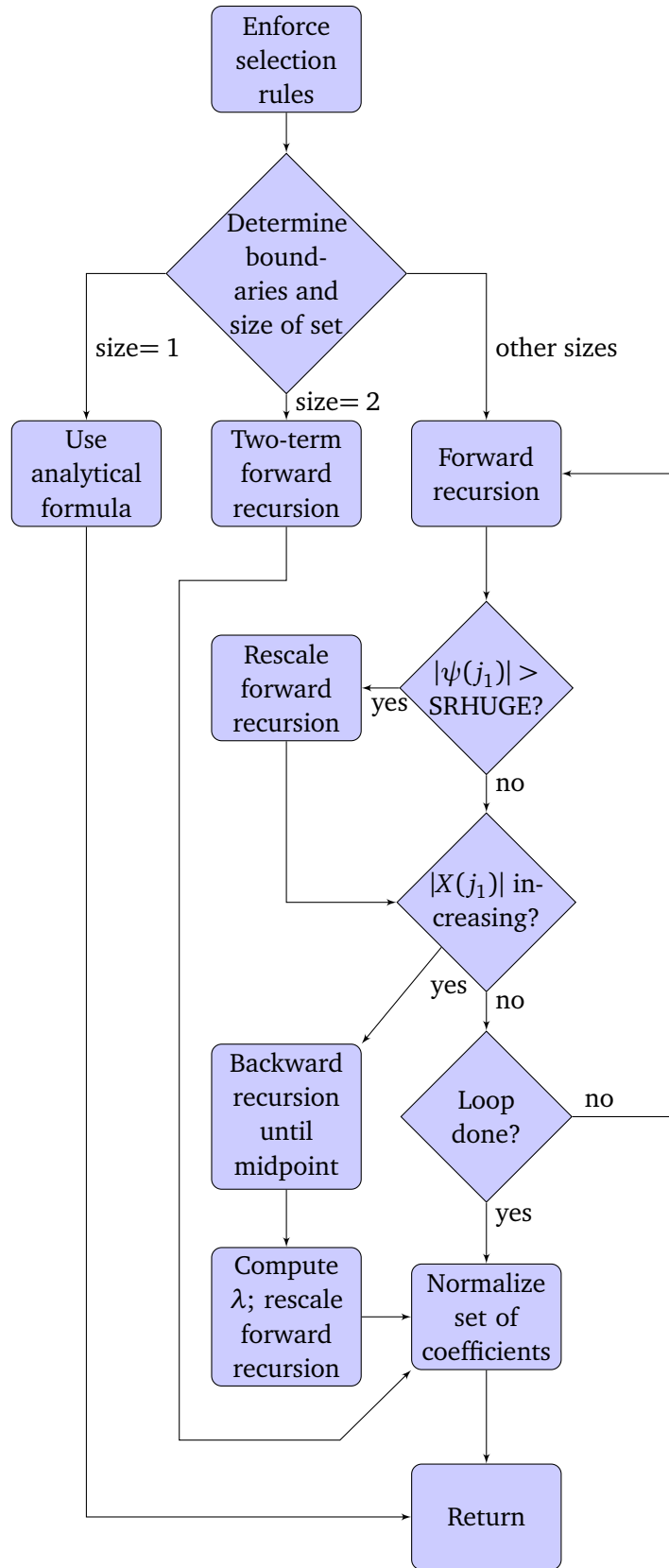


Figure C.4 – Flowchart of the algorithm used to compute the coupling coefficients. SRHUGE is the square root of the biggest representable number in our floating point representation.

Table C.1 – Parameters and coefficients of the three-term recursion relations satisfied by the $3j$ - and $6j$ -symbols. The expression $[++-]$ represents the coefficient $[j_1(j_1+1)+j_2(j_2+1)-j_3(j_3+1)]$ and similarly for other signs in the bracket.

$3j$ - or $6j$ - symbols	$f(j_1) = \begin{pmatrix} j_1 & j_2 & j_3 \\ m_1 & m_2 & m_3 \end{pmatrix}$	$h(j_1) = \begin{Bmatrix} j_1 & j_2 & j_3 \\ j_4 & j_5 & j_6 \end{Bmatrix}$
α_ψ	$j_1 A(j_1 + 1)$	$j E(j_1 + 1)$
β_ψ	$B(j_1)$	$F(j)$
γ_ψ	$(j_1 + 1)A(j_1)$	$(j_1 + 1)E(j)$
Functions	$A(j_1) = [j_1^2 - (j_2 - j_3)^2]^{1/2}$ $\times [(j_2 + j_3 + 1)^2 - j_1^2]^{1/2}$ $\times [j_1^2 - m_1^2]^{1/2}$	$E(j_1) = \{[j_1^2 - (j_2 - j_3)^2]$ $\times [(j_2 + j_3 + 1)^2 - j_1^2]$ $\times [j_1^2 - (j_5 - j_6)^2]$ $\times [(j_5 + j_6 + 1)^2 - j_1^2]\}^{1/2}$
	$B(j_1) = -(2j_1 + 1)$ $\times [j_2(j_2 + 1)m_1$ $- j_3(j_3 + 1)m_1$ $- j_1(j_1 + 1)(m_3 - m_2)]$	$F(j_1) = (2j_1 + 1)$ $\times \{j_1(j_1 + 1)[- - +]$ $+ j_5(j_5 + 1)[+ + -]$ $+ j_6(j_6 + 1)[+ - +]$ $- 2j_1(j_1 + 1)l_1(l_1 + 1)\}$
Endpoints	$j_{1\min} = \max(j_2 - j_3 , m_1)$ $j_{1\max} = j_2 + j_3$	$j_{1\min} = \max(j_2 - j_3 , j_5 - j_6)$ $j_{1\max} = \min(j_2 + j_3, j_5 + j_6)$
Normalization	$\sum_{j_1} (2j_1 + 1) f(j_1)^2 = 1$	$(2j_4 + 1) \sum_{j_1} (2j_1 + 1) h(j_1)^2 = 1$
Sign	$\text{sgn}[f(j_{1\max})] = (-1)^{j_2 - j_3 - m_1}$	$\text{sgn}[h(j_{1\max})] = (-1)^{j_2 + j_3 + j_5 + j_6}$

spherical harmonics.

C.4.1 Definition of the scalar and vector spherical harmonics

While there is a number of ways to introduce the spherical harmonics, we will take the top to bottom approach: from the general to the specific. In all generality, spherical harmonics are solutions of the equation

$$[\nabla_\Omega^2 + \ell(\ell + 1)] Y_{jm}^{\ell S}(\theta, \varphi) = 0 \quad (\text{C.29})$$

where $Y_{jm}^{\ell S}$ is actually a *tensor* spherical harmonic. It describes the angular distribution and polarization of spin- S particles with angular momentum j , projection m and orbital angular momentum ℓ [42]. While the study of particles with arbitrary spin S is interesting in its own right, we will concentrate on the case of particles of spin-1 and their scalar approximation (spin-0). Since the values of ℓ range from $|J - S|$ to $J + S$, the spin-0 case reduces to the usual scalar spherical har-

monics while the spin-1 case are the *vector* spherical harmonics. As said in the main text, they can be formed by a superposition of scalar spherical harmonics of the form

$$Y_{jm}^\ell(\theta, \varphi) = \sum_{m', \sigma} C_{lm', 1\sigma}^{jm} Y_\ell^{m'}(\theta, \varphi) \hat{e}_\sigma \quad (\text{C.30})$$

The numerical evaluation of these functions are then contingent on the evaluation of the scalar spherical harmonics and the Clebsch-Gordan coefficients. The first was covered in the previous appendix and we will soon tend to the second.

The scalar spherical harmonics can simply be written as

$$Y_\ell^m(\theta, \varphi) = P_\ell^m(\cos \theta) e^{im\varphi} \quad (\text{C.31})$$

where P_ℓ^m is the normalized version of the associated Legendre polynomials [39]. They are related to the usual Legendre polynomials \tilde{P}_ℓ^m through

$$P_\ell^m(x) = \sqrt{\frac{2\ell+1}{4\pi} \frac{(\ell-m)!}{(\ell+m)!}} \tilde{P}_\ell^m(x) \quad (\text{C.32})$$

To numerically evaluate the spherical harmonics, then, we must safely evaluate the associated Legendre polynomials. One of the only stable recurrence relation is [39]

$$P_\ell^m(x) = \sqrt{\frac{4\ell^2-1}{\ell^2-m^2}} \left[x P_{\ell-1}^m(x) - \sqrt{\frac{(\ell-1)^2-m^2}{4(\ell-1)^2-1}} P_{\ell-2}^m(x) \right] \quad (\text{C.33})$$

The initial conditions are provided by

$$P_m^m(x) = (-1)^m \sqrt{\frac{2m+1}{4\pi(2m)!}} (2m-1)!! (1-x^2)^{m/2} \quad (\text{C.34})$$

$$P_{m+1}^m(x) = x \sqrt{2m+3} P_m^m(x) \quad (\text{C.35})$$

At first sight, it might seem dangerous to evaluate $P_m^m(x)$ because of the division of two factorial functions. However, by taking the square of the expression and looking at the factorial functions, we have

$$a_m = \frac{[(2m-1)!!]^2}{(2m)!}. \quad (\text{C.36})$$

This can be evaluated rather simply by noting that $(2m-1)!! = (2m)!/2^m m!$. Rearranging, we get

$$a_m = \frac{(2m)!}{2^{2m}(m!)^2} = \frac{1}{2^{2m}} \binom{2m}{m}.$$

We further notice that

$$\frac{a_{m+1}}{a_m} = \frac{2^{2m}}{2^{2(m+1)}} \frac{\binom{2(m+1)}{m+1}}{\binom{2m}{m}} = \frac{2m+1}{2m+2}. \quad (\text{C.37})$$

We can then safely evaluate $P_m^m(x)$ using the formula

$$P_m^m(x) = \sqrt{\frac{2m+1}{4\pi} \prod_{i=0}^{m-1} \frac{2i+1}{2i+2}} (1-x^2). \quad (\text{C.38})$$

Our numerical implementation shows machine precision for all spherical harmonics up to $\ell = 3$ (we compared the results of our algorithm with the analytical forms of the spherical harmonics). Moreover, we tested our algorithm against the following sums [42, §5.10]

$$\sum_m |Y_\ell^m(\theta, \varphi)|^2 = \frac{2\ell+1}{4\pi} \quad (\text{C.39})$$

$$\sum_m m |Y_\ell^m(\theta, \varphi)|^2 = 0 \quad (\text{C.40})$$

$$\sum_m m^2 |Y_\ell^m(\theta, \varphi)|^2 = \frac{\ell(\ell+1)(2\ell+1)}{8\pi} \sin^2 \theta. \quad (\text{C.41})$$

They are verified to a precision of 10^{-7} up to $\ell = 500$. The uncertainty on the sums grows with ℓ . Figure C.5 tells us that the spherical harmonics are computed near to or at machine precision (in `double`). The increasing error is due to error accumulation. At large ℓ , there are a lot of terms to sum, thus increasing the absolute error made in the computation.

C.4.2 Spherical Harmonics Transform

While the Fast Fourier Transform has had hundreds of experts working on it, this is not true of the Fast Spherical Harmonics Transform. The program libraries are scarce and, for the most part, still in their infancy. This is in sharp contrast with the FFT case, where numerous libraries provide algorithms that performs FFTs at a cost of $\mathcal{O}(n \log n)$. FFTW is an example of such a mature, robust program library.

Any smooth function can be expanded in a spherical harmonics series (they form a complete basis on the 2-sphere) with [39, §6.7.1]

$$f(\theta, \varphi) = \sum_{\ell=0}^{\ell_{\max}} \sum_{m=-\ell}^{\ell} a_{\ell m} P_\ell^m(\cos \theta) e^{im\varphi} \quad (\text{C.42})$$

Using the orthonormality conditions, we can find an expression for the expansion coefficients

$$a_{\ell m} = \iint_{\Omega} f(\theta, \varphi) e^{-im\varphi} P_\ell^m(\cos \theta) \sin \theta d\theta d\varphi \quad (\text{C.43})$$

In the discrete case, then, the integral becomes a quadrature

$$a_{\ell m} = \sum_{i,j} w(\theta_i) f(\theta_i, \varphi_j) e^{-im\varphi_j} P_\ell^m(\cos \theta_i). \quad (\text{C.44})$$

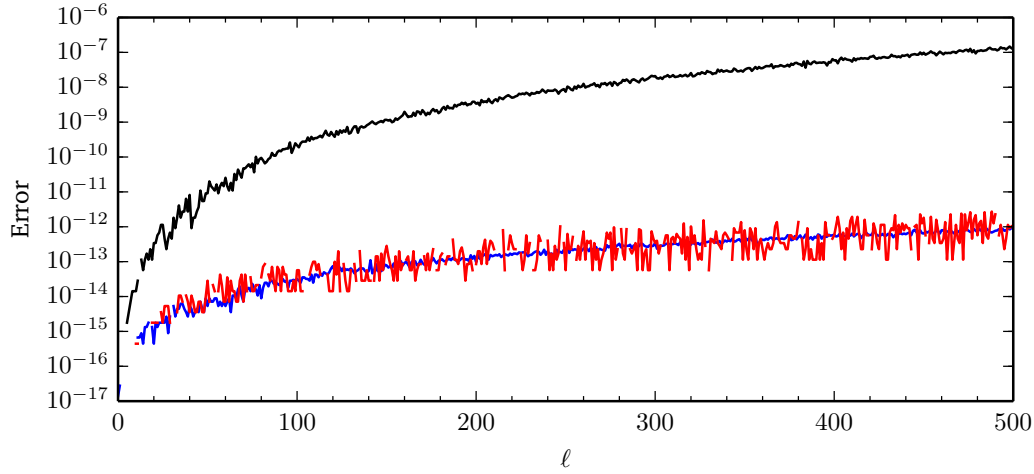


Figure C.5 – Precision of our implementation of the algorithm that evaluates the spherical harmonics. The blue curve corresponds to (C.39), the red curve to (C.40) and the black curve to (C.41).

The fastest way to perform the quadrature over φ_j is, of course, to use the FFT. We will perform the quadrature over θ_i by using a Gauss-Legendre quadrature. While the cost of such an algorithm is the worst we could get ($\mathcal{O}(\ell^3)$), it is also the easiest to implement. Faster transforms are available in the literature [49–51].

To find the abscissas of the Gauss-Legendre quadrature (the roots of $P_\ell^0(\cos \theta)$), we perform a few rounds of Newton-Raphson using the following initial guess on the positions of the zeros [37]

$$\xi_{\ell,k} = \left(1 - \frac{1}{8\ell^2} + \frac{1}{8\ell^3}\right) \cos\left(\frac{4k-1}{4\ell+2}\pi\right) + \mathcal{O}(\ell^{-4}) \quad (\text{C.45})$$

where $\xi_{\ell,k}$ is the k th root (ordered in $[-1, 1]$) of $P_\ell^0(\cos \theta)$.

Bibliography

- [1] J. W. Strutt (Lord Rayleigh), *Theory of Sound*, vol. II (MacMillan, London, 1878).
- [2] J. W. Strutt (Lord Rayleigh), “The Problem of the Whispering Gallagery,” *Philos. Mag.* **20**, 1001–1004 (1910).
- [3] O. Wright, “Gallery of whispers,” *Phys. World* pp. 31–36 (2012).
- [4] Y. Yamamoto and R. E. Slusher, “Optical Processes in Microcavities,” *Phys. Today* **46**, 66 (1993).
- [5] A. Serpengüzel, S. Arnold, and G. Griffel, “Excitation of resonances of microspheres on an optical fiber,” *Opt. Lett.* **20**, 654–656 (1995).
- [6] F. Vollmer, D. Braun, A. Libchaber, M. Khoshsim, I. Teraoka, and S. Arnold, “Protein detection by optical shift of a resonant microcavity,” *Appl. Phys. Lett.* **80**, 4057 (2002).
- [7] D. K. Armani, T. J. Kippenberg, S. M. Spillane, and K. J. Vahala, “Ultra-high-Q toroid microcavity on a chip,” *Nature* **421**, 925–8 (2003).
- [8] F. Vollmer and S. Arnold, “Whispering-gallery-mode biosensing: label-free detection down to single molecules,” *Nat. Methods* **5**, 591–596 (2008).
- [9] G. Painchaud-April, “Dielectric Cavities: Scattering Formalism and Applications,” Ph. d. thesis, Université Laval.
- [10] J. D. Jackson, *Classical Electrodynamics* (John Wiley & Sons, 1962).
- [11] H. G. L. Schwefel, “Directionality and Vector Resonances of Regular and Chaotic Dielectric Microcavities,” Ph. d. thesis, Yale University (2004).
- [12] R. Dubertrand, E. Bogomolny, N. Djellali, M. Lebental, and C. Schmit, “Circular dielectric cavity and its deformations,” *Phys. Rev. A* **77**, 013804 (2008).
- [13] S. Bittner, E. Bogomolny, B. Dietz, M. Miski-Oglu, P. Oria Iriarte, A. Richter, and F. Schäfer, “Experimental test of a trace formula for two-dimensional dielectric resonators,” *Phys. Rev. E* **81**, 066215 (2010).

- [14] C. P. Dettmann, G. V. Morozov, M. Sieber, and H. Waalkens, “Unidirectional emission from circular dielectric microresonators with a point scatterer,” *Phys. Rev. A* **80**, 063813 (2009).
- [15] J. A. Stratton, *Electromagnetic Theory* (McGraw-Hill Book Company, 1941).
- [16] F. T. Smith, “Lifetime Matrix in Collision Theory,” *Phys. Rev.* **118**, 349–356 (1960).
- [17] L. Eisenbud, “The Formal Properties of Nuclear Collisions,” Ph. d., Princeton University (1948).
- [18] C. A. A. de Carvalho and H. M. Nussenzveig, “Time delay,” *Phys. Rep.* **364**, 83–174 (2002).
- [19] R. G. Newton, *Scattering Theory of Waves and Particles* (Springer-Verlag, New York, 1982), 2nd ed.
- [20] A. I. Rahachou and I. V. Zozoulenko, “Scattering Matrix Approach to the Resonant States and Q Values of Microdisk Lasing Cavities,” *Appl. Opt.* **43**, 1761–1772 (2004).
- [21] M. Greenberg, *Advanced Engineering Mathematics* (Pearson, 1998).
- [22] M. I. Mishchenko, L. D. Travis, and A. A. Lacis, *Scattering, Absorption and Emission of Light by Small Particles* (Cambridge University Press, 2002), 3rd ed.
- [23] H. E. Türeci, “Wave Chaos in Dielectric Resonators : Asymptotic and Numerical Approaches,” Ph. d. thesis, Yale University (2003).
- [24] M. Hentschel and K. Richter, “Quantum chaos in optical systems: The annular billiard,” *Phys. Rev. E* **66**, 056207 (2002).
- [25] V. A. Toponogov, *Differential Geometry of Curves and Surfaces: A Concise Guide* (Birkhäuser, 2005), 1st ed.
- [26] B. Schutz, *A First Course in General Relativity* (Cambridge University Press, 2009), 2nd ed.
- [27] R. S. Elliott, *Antenna Theory and Design*, IEEE Press Series on Electromagnetic Wave Theory (Wiley-Interscience, 2003), revised ed.
- [28] L. Novotny and B. Hecht, *Principles of Nano-Optics* (Cambridge University Press, 2012), 2nd ed.
- [29] J. R. de Lasson, J. Mørk, and P. T. s. Kristensen, “Three-dimensional integral equation approach to light scattering, extinction cross sections, local density of states, and quasi-normal modes,” *J. Opt. Soc. Am. B* **30**, 1996 (2013).
- [30] L. M. Delves and J. L. Mohamed, *Computation Methods for Integral Equations* (Cambridge University Press, 1985).

- [31] A. Ben-Menahem and S. J. Singh, "Eigenvector Expansions of Green's Dyads with Applications to Geophysical Theory," *Geophys. J. Int.* **16**, 417–452 (1968).
- [32] "Std. 145-1993," IEEE Stand. Defin. Terms Antennas. p. 40 (1993).
- [33] J. H. Wang and K. K. Mei, "Theory and analysis of leaky coaxial cables with periodic slots," *IEEE Trans. Antennas Propag.* **49**, 1723–1732 (2001).
- [34] D. K. Cheng, *Field and Wave Electromagnetics* (Addison-Wesley, 1989), 2nd ed.
- [35] R. Landauer, "Electrical conductivity in inhomogeneous media," in "AIP Conf. Proc.", , vol. 40 (AIP, 1978), vol. 40, pp. 2–45.
- [36] K. Mitzner, "Effective boundary conditions for reflection and transmission by an absorbing shell of arbitrary shape," *IEEE Trans. Antennas Propag.* **16**, 706–712 (1968).
- [37] M. Abramowitz and I. A. Stegun, *Handbook of Mathematical Functions* (Dover Publications, 1965).
- [38] A. Cuyt, V. B. Petersen, B. Verdonk, H. Waadeland, and W. B. Jones, *Handbook of Continued Fractions for Special Functions* (Springer, 2008).
- [39] W. H. Press, S. A. Teukolsky, W. T. Vetterling, and B. P. Flannery, *Numerical Recipes : the Art of Scientific Computing* (Cambridge University Press, 2007), 3rd ed.
- [40] N. M. Temme, "The numerical computation of the confluent hypergeometric function $U(a, b, z)$," *Numer. Math.* **41**, 63–82 (1983).
- [41] I. Thompson and A. Barnett, "Coulomb and Bessel functions of complex arguments and order," *J. Comput. Phys.* **64**, 490–509 (1986).
- [42] D. A. Varshalovich, A. N. Moskalev, and V. K. Khersonskii, *Quantum Theory of Angular Momentum: Irreducible Tensors, Spherical Harmonics, Vector Coupling Coefficients, 3nj Symbols* (World Scientific, 1988).
- [43] D. M. Brink and G. R. Satchler, *Angular Momentum* (Oxford University Press, 1993), 3rd ed.
- [44] C. Cohen-Tannoudji, B. Diu, and F. Laloë, *Mécanique quantique*, vol. 2 (Hermann, 1973).
- [45] A. P. Yutsis, I. B. Levinson, and V. V. Vanagas, *Mathematical Apparatus of the Theory of Angular Momentum* (Israel Program for Scientific Translations, Jerusalem, 1962).
- [46] K. Schulten, "Exact recursive evaluation of 3j- and 6j-coefficients for quantum-mechanical coupling of angular momenta," *J. Math. Phys.* **16**, 1961 (1975).
- [47] K. Schulten and R. Gordon, "Recursive evaluation of 3j and 6j coefficients," *Comput. Phys. Commun.* **11**, 269–278 (1976).

- [48] J. Luscombe and M. Luban, “Simplified recursive algorithm for Wigner 3j and 6j symbols,” *Phys. Rev. E* **57**, 7274–7277 (1998).
- [49] V. Rokhlin and M. Tygert, “Fast Algorithms for Spherical Harmonic Expansions,” *SIAM J. Sci. Comput.* **27**, 1903–1928 (2006).
- [50] M. Tygert, “Fast algorithms for spherical harmonic expansions, II,” *J. Comput. Phys.* **227**, 4260–4279 (2008).
- [51] M. Tygert, “Fast algorithms for spherical harmonic expansions, III,” *J. Comput. Phys.* **229**, 6181–6192 (2010).

Index

- boundary conditions
 - electromagnetic, 7
- constitutive relations, 6
- continued fraction expansions, **51–54**
 - numerical evaluation of, 52
- dielectric resonators, 1
- left eigenvectors, 17
- scattering matrix, 14